2021-01-13

Bay-region Expanded Perylene Diimides for Green Printed Electronics

Harris, Dylan Henry

UNIVERSITY OF CALGARY

Bay-region Expanded Perylene Diimides for Green Printed Electronics

by

Dylan Henry Harris

A THESIS

SUBMITTED TO THE FACULTY OF GRADUATE STUDIES

IN PARTIAL FULFILMENT OF THE REQUIREMENTS FOR THE

DEGREE OF MASTER OF SCIENCE

GRADUATE PROGRAM IN CHEMISTRY

CALGARY, ALBERTA

JANUARY, 2021

Abstract

Reported within is the development of a new acid-catalyzed synthesis that provides access to alcohol-processable bay-substituted N-H functionalized PDI derivatives. The results were published in a recent manuscript[55] and have been included in Chapters 1 and 2 of this thesis. Full structural and optoelectronic characterization was performed including optical absorption spectroscopy, cyclic voltammetry (CV), single crystal X-ray diffraction (SC-XRD), ^{1}H-NMR spectroscopy, ^{13}C-NMR spectroscopy, MALDI-TOF mass spectrometry, CHN elemental analysis, thermogravimetric analysis (TGA) and differential scanning calorimetry (DSC). Molecular design considerations are presented in the context of density functional theory (DFT) energy level diagrams from collaborators in the Rondeau-Gagné lab at University of Windsor. Organic field effect transistor (OFET) device data was collected *via* our collaboration with the Lessard lab at University of Ottawa. This thesis strives to highlight multiple ways in which our new synthetic method can be utilized to provide high performing and green solvent processable OFET materials. Successes and failures of the synthesis of new targets are documented and discussed with respect to electronic structure considerations.

Preface

This thesis is original, unpublished, independent work by the author Dylan Henry Harris, with exception of Chapters 1 and 2 in which work was included from a previously published manuscript *J. Mater. Chem. C.,* 2020, **8** (29), 9811–9815 of which I am the first author.

Table of Contents

List of Figures

List of Abbreviations and Symbols

BCF = Tris(pentafluorophenyl)borane

CV = cyclic voltammetry

DEPT = distortionless enhancement by polarization transfer

DPV = differential pulse voltammetry

DSC = differential scanning calorimetry

EtOAc = Ethyl acetate

GreEN = NSERC green electronics network

HOMO = highest occupied molecular orbital

LUMO = lowest occupied molecular orbital

MALDI-TOF = matrix assisted laser desorption/ionization – time of flight

NMR = nuclear magnetic resonance

OFET = organic field effect transistor

PDI = Perylene diimide

PL = photoluminescence

TFA = Trifluoroacetic acid

TfOH = Trifluoromethanesulfonic acid

TGA = thermogravimetric analysis

THF = Tetrahydrofuran

TsOH•H_2O = *p*-Toluenesulfonic acid monohydrate

XRD = X-ray diffraction

μ = electron mobility (units: $cm^2\ V^{-1}\ s^{-1}$)

1. Introduction

1.1. Project Goal

Develop a new series of organic π-conjugated materials that can be used to deliver high electron mobility organic field effect transistors following green chemistry principles. Collaborations will be required to acquire electronic structure information and electron mobility values. This project was developed for and funded by the NSERC Strategic Network – Green Electronics Network (GreEN).

1.2. Hypothesis

Use the PDI conjugated building block to develop a new class of molecules to achieve the goal. The PDI chromophore is electron deficient leading to suitable electronic energy levels to transport electrons in the bulk and inject electrons into relevant electrodes. PDI has a planar aromatic structure allowing for strong π-π stacking that can lead to an organized nanomorphology in the solid-state required for high electron transport. Incorporate NH functional groups to allow for deprotonation (salt formation) which is known to increase a material's polar solvent solubility, and thus enable eco-friendly solvent processing.

1.3. PDI Materials for Use in Organic Electronics

PDIs have been widely used to construct organic semiconductors for use as the active material in organic field-effect transistors (OFETs).[1-5] The high electron affinity allows for facile electron injection from low work function metals while the polycyclic aromatic backbone enables close intermolecular π-π stacking conducive to rapid electron transport.[6,7] The two 'imide' positions of PDI can be seen in Figure 1 denoted by R groups. The imide position can be varied, as the R group is dependent on the amine that is used for the imidization reaction (Fig. 1 (A)). Different imide groups can be chosen to effect desirable solubility characteristics and effect the self-assembly and packing of the PDI molecules. The 'bay' positions of PDI are denoted 1,6,7, and 12 in Figure 1 (B). In order to functionalize the bay position(s) of PDI, these positions are often brominated via the use of liquid bromine.[8] Conversely the bay position(s) can also be nitrated via the use of fuming nitric acid. Both of these electrophilic aromatic substitution reactions are very robust and provide access to various PDI analogues. The synthesis of the 1,7-dibromo PDI precursor is investigated at length in the literature as it is often found that the bromination reaction of PDI produces an isomeric mixture of 1,6 and 1,7-bromo PDIs, though this can be solved by brominating the perylene dianhydride precursor rather than PDI.[9] The last positions of importance are known as the 'headland' positions and are denoted 2,5,8, and 11 in Figure 1 (B).

The optical absorption spectrum of PDI displays three strong vibronic absorption bands at ≈500 nm. It is notable that the absorption spectrum is rarely affected by varying the imide substituent alone. A nodal plane exists between the imide and perylene core negating electronic communication, thus no major change in molecular properties is expected. It is often necessary to introduce electron donating substituents at the bay position(s) in order to disrupt the vibronic nature of PDI. Cyclic voltammetry (CV) of PDI can be used to understand its redox character, and

to predict the highest occupied molecular orbital and lowest occupied molecular orbital (HOMO and LUMO, respectively) energy levels of the material. PDI displays two reduction events, spaced close together, and zero oxidation events in its cyclic voltammogram. Lowering the LUMO energy level is of great importance to developing an air-stable high-performing organic semiconductor. If the LUMO energy level is too high an electron can transfer to O_2, forming the superoxide anion

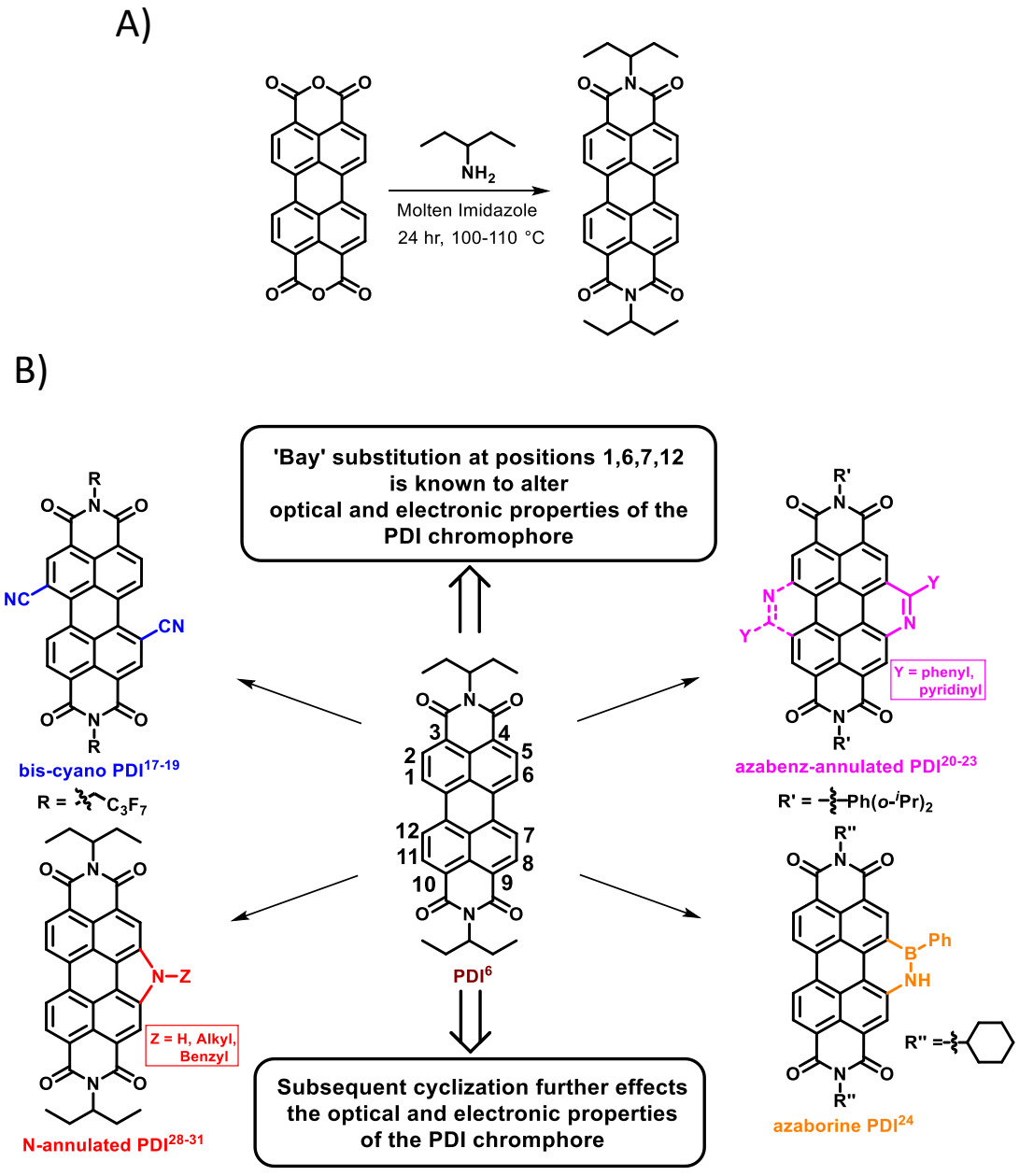

Figure 1: A) Synthesis of PDI. B) Structure-Property relationships of PDI derivatives

O_2^- which can degrade the material. Unsubstituted PDI can be challenging to work with due to poor solubility in a variety of solvents, as a consequence of strong π-π stacking. Chlorinated solvents are frequently required to dissolve unsubstituted PDIs, presenting a synthetic challenge to modify PDI in a way which can increase solubility providing a greater range of solvents to select from for solution processing. Solution processing conditions can have a major impact on the self-assembly of the molecules in the solid state, leading to different performance.

Various fluorinated PDIs with very high electron affinities can form stable radical anions allowing for air stable OFET operation.[10-12] A myriad of structures has been reported and studied in the realm of OFETs[13-15] with high electron mobilities being demonstrated.[16] Most notably the bis-cyano derivative is the top performing solution processed PDI organic semiconductor[17-19] (Fig. 1). Synthesis is achieved via 1,7-dibromination of perylene dianhydride followed by imidization using the appropriate fluoroalkyl amine precursor. The dibrominated PDI derivative is then subjected to aromatic cyanation conditions using zinc cyanide and tris(dibenzylideneacetone)dipalladium(0) ($Pd_2(dba)_3$), although it is notable that a phosphine ligand is not necessary for the reaction (reported yield: 80%). The optical absorption spectrum of the bis-cyano PDI structure in Fig. 1 displays strong vibronic coupling at approximately 500 nm. Cyclic voltammetry results show that reduction potentials of the bis-cyano PDI derivative are lower than comparative PDI derivatives which do not contain electron withdrawing groups. This is an important point to understand for designing n-type synthetic targets. The ability to introduce electron withdrawing groups via the imide position and the bay position(s) of PDI allows for the design and synthesis of organic semiconductors which will possess ideal redox potentials for device operation. Furthermore, the LUMO and HOMO energy levels were determined to be -4.5 eV and -6.8 eV, respectively. It is important to note that not only is high device performance

important, but it is also pivotal to develop air-stable organic semiconductors. Lastly, these cyano PDI derivatives are soluble in organic solvents alone, which poses a challenge for eco-friendly processing. OFET results show that this compound has mobilities of 0.27 $cm^2 V^{-1}s^{-1}$ under vacuum and 0.24 $cm^2 V^{-1}s^{-1}$ in air.

An effective method to modify PDI is ring expansion (Fig. 1 (B)). Condensation of boranes or aldehydes with the amino functionalized PDI to give the azabenz-annulated[20-23] or azaborine PDIs,[24] can lead to altering of optical, electrochemical, and self-assembly tendencies. Azabenz-annulated PDIs can be synthesized via amine condensation to give the imine, immediately followed by cyclization/oxidative rearomatization. Unlike the 1,7-dibromination discussed earlier, the 1,7-dinitration of PDI needed to obtain the amino precursor is shown to produce exclusively the desired 1,7-dinitro regioisomer. It is noted that Hudhomme and co-workers recently expanded the synthetic method to include bis-azabenz-annulated PDIs.[23] The optical absorption spectrum of azabenz-annulated PDIs displays a slight redshift when compared to the parent PDI, with a distinct band at approximately 350 nm as a consequence of core-extension.[25-27] CV results show that azabenz-annulated PDIs display two reduction events and zero oxidation events. It is shown that incorporating a nitrogen into the azabenz-annulated PDI structure does not significantly affect the electrochemical behaviour. The LUMO energy levels of the azabenz-annulated PDI derivatives range from -3.82 eV to -3.88 eV, lower than that of unfunctionalized PDI, indicating that this strategy is effective in tuning the band gap. Solubility of these compounds is not discussed in length and all processing is performed in chlorinated solvents, indicating that these molecules are not soluble in more eco-friendly solvents. OFET device data is currently unavailable for this class of compounds.

The synthesis of azaborine PDI[24] (Fig. 1 (B)) is performed in a similar fashion to azabenz-annulated PDIs. Amino PDI is utilized to facilitate a condensation with the electron deficient organoborane species dichlorophenylborane, followed by cyclization. The optical absorption spectrum of azaborine PDI displays a strong absorption maximum at 529 nm and a shoulder at 427 nm. The spectrum is redshifted in comparison to its carbon-based analogue due to the strong dipole moment of the B-N bond compared to the weaker dipole moment of a C=C bond. Interestingly, CV results show that the azaborine derivative possesses three reversible reduction events and zero oxidation events. The LUMO energy level of azaborine PDI was determined to be -3.63 eV. Experimental data shows that azaborine PDI is soluble in DMF and chloroform, although the degree of solubility in other solvents is not discussed. OFET device data is not available for azaborine PDI, its major application thus far has been for OLEDs.

Our design strategy is focused on the development of monomeric PDI molecules with functional N-H bonds. N-annulated PDIs[28-31] (Fig. 1 (B)) have been previously reported and have polar N-H bonds that impart the PDI chromophore with distinct properties when compared to the parent unfunctionalized PDI.[6] The N-annulated PDI maintains the distinct red colour of PDI but has destabilised HOMO and LUMO energy levels, making it harder to reduce[32] while the NH group can be polarized by bases[33] and/or functionalized with alkyl side chains dramatically improving materials solubility.[34] N-annulated PDI synthesis begins in a similar fashion to azaborine and azabenz-annulated PDIs with the nitration of PDI. Nitro PDI can then be cyclized to form a 5 membered nitrogen ring via the use of triphenylphosphine as a catalyst. Once unfunctionalized N-annulated PDI (i.e. Z=H) is obtained, the free amine can either be polarized with a base or functionalized with alkyl or aryl substituents to improve solubility in desirable solvents. Work is currently ongoing for OFET device testing of these molecules.

1.4. Green Solvent Processing

By far most of the solution processed OFETs make use of halogenated or aromatic solvents for film formation via solution processing. As OFET technology moves towards commercialization in a range of electronic devices, there is a need to develop new organic semiconductors that can be processed into ordered films with good electron mobility from green solvents (e.g. water, alcohols, acetates).[35-38] Use of such green solvents reduces negative human and environmental impact caused by large-scale manufacturing.[39,40] Figure 2 displays previously reported strategies that have been implemented to improve the green solvent solubility of PDI materials including: 1- ionic side chains[41,42]; 2- glycol side chains[43]; 3- zwitterionic side chains[44]; 4 – polarizable N-H[45]. Furthermore, ionic chains have been used to facilitate aqueous processing of PDI-based organic semiconductors.[46-48] Such side-chain engineering can dramatically improve green solvent solubility but can hinder organized molecular self-assembly. In an effort to understand the relationship between self-assembly and the nature of the side-chain, various side-chains have been investigated and incorporated into several different π-conjugated aromatic

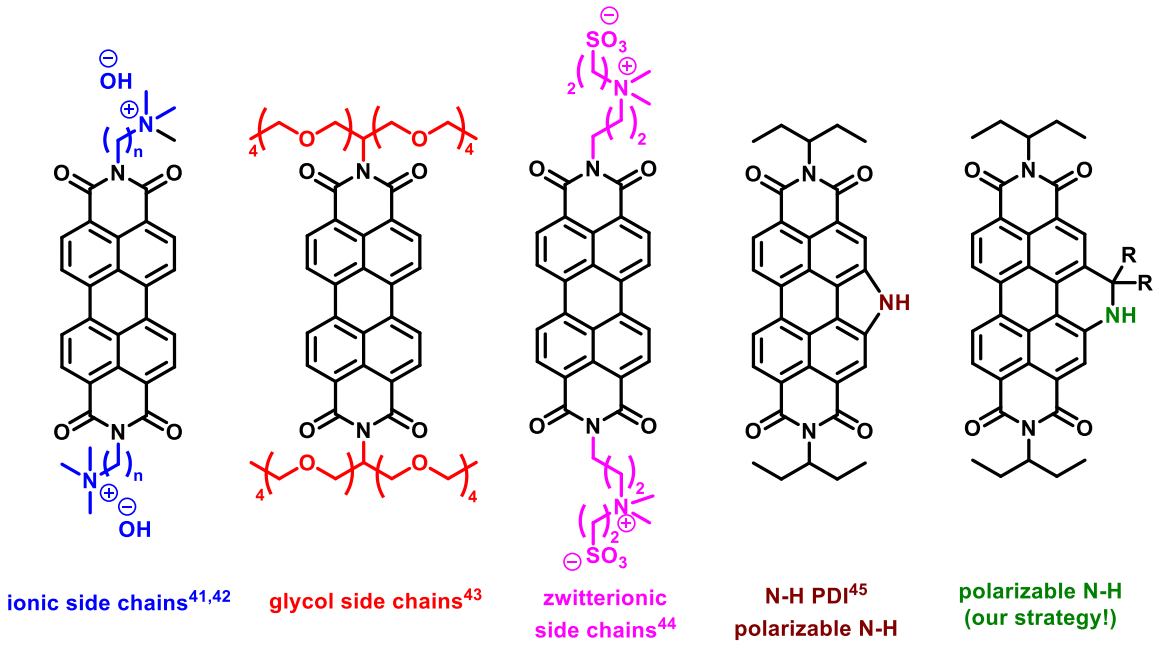

Figure 2: Several strategies available for enabling green solvent processed OFETs

cores[49-52]. We report a simple strategy that incorporates a N-H bond in the form of a 6-membered cyclic secondary amine at the bay position of the PDI chromophore (Fig. 3). By avoiding large ionic side chains, we hope to improve green solvent solubility without harming desirable self-assembly characteristics. The product contains a N-H bond which is suspectable to polarization via interactions with bases, enabling eco-friendly solvent solubility (Fig. 3). This work was inspired by previous work from our laboratory on the N-H PDI[45] molecule shown in Figure 2. The process outlined in Figure 3 shows how the N-H bond can be polarized with a base to dramatically increase green solvent solubility. When film formation occurs, the volatile base evaporates and the negatively charged nitrogen is protonated to revert the molecule back to its original form. Also, in the solid-state intermolecular H-bonding interactions can occur and stabilize the neutral N-H species. This is the process that we are hoping to exploit to improve green solvent solubility without harming the overall performance of the resultant organic semiconducting thin-film.

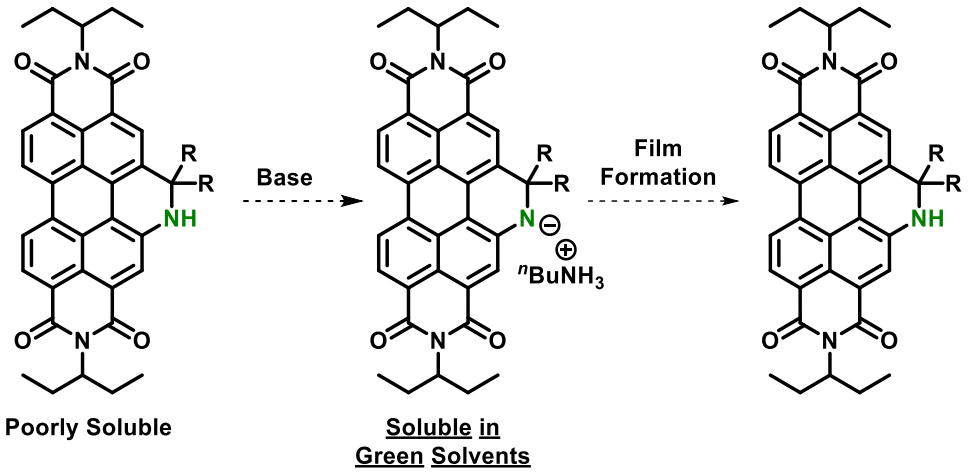

Figure 3: Mechanism of film formation from green solvents *via* polarization of the N-H bond with base, the base is typically a primary amine

1.5. Field of Organic Electronics

The field of organic electronics is focused on the design, synthesis, and processing of organic semiconductors into devices. One such device is an OFET, which can be used in temperature or time sensors due to its ability to monitor changes in electrical signals. The main physical property which is used to gauge the performance of an OFET is the electron mobility (μ). Focus of this thesis will be on n-type OFETs. Figure 4 displays the general architecture of a n-type OFET and explains my overall role in its fabrication.

The predominant processing method for organic electronics is solution processing, which requires solubilizing the organic semiconductor and subsequently forming an organic thin-film using a deposition process (spin-coating, slot-die coating, ink-jet printing, etc.). Solution processing is primarily used because it can be performed at a room temperature, allowing for the formation of thin-films with low energy demand. Additionally, solution processing allows for low-temperature deposition on plastic substrates that would be melted using high-temperature processing conditions. The ability to solution process organic films is a main advantage of organic electronics. Our objective will be to design and synthesize organic semiconductors which can be solution processed in an eco-friendly manner.

A major challenge that has been presented thus far is the need to process organic semiconductors from eco-friendly solvents. This thesis will attempt to improve upon the processing methods used to fabricate organic thin films by designing synthetic targets that are intrinsically soluble in green solvents or ones that can be chemically altered to become soluble. The series of solvents that will be investigated will include: 2-Methyltetrahydrofuran, Ethyl acetate, *n*-propanol, and water. Characterization methods including: optical absorption spectroscopy, CV, single crystal XRD, ^{1}H-NMR spectroscopy, ^{13}C-NMR spectroscopy, MALDI-

TOF mass spectrometry, CHN elemental analysis, TGA and DSC will be executed in order to understand the optoelectronic, thermal, and self-assembly properties of the synthesized materials.

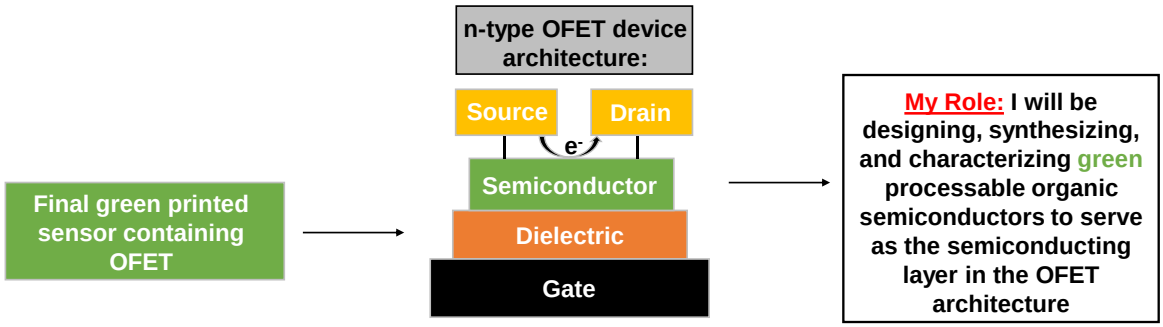

Figure 4: Schematic explaining my role in developing an OFET device

2. X1: A New N-H Functionalized PDI

2.1. Design and Synthesis of X1

Amino PDI (PDI-NH2, **1**, Fig. 5)[53,54] has been previously reported and its physical, optical, and electronic properties have been determined. **1** has a distinct blue colour owing to strong charge transfer from the electron rich amine to the electron poor PDI core. Like N-annulated PDI, **1** also possesses polar N-H bonds which helps increase its solubility in polar solvents through deprotonation.

The synthesis of the target compound **X1**,[55] is shown in Figure 5. The synthetic pathway is similar to that previously reported to make azabenz-annulated PDIs[20-23] but makes use of a ketone instead of the aldehyde to prevent oxidative rearomatization, affording the final PDI chromophore with a N-H functionality.

Table 1 shows the optimization of the acid-catalyzed condensation reaction. In the synthesis of previously reported azabenz-annulated PDIs[20-23] trifluoroacetic acid (TFA) was used as the acid catalyst. Attempts with TFA as the catalyst (entries 1 and 2) were unsuccessful. This may be due to a key difference in our method to that of the azabenz-annulated PDI synthesis. In

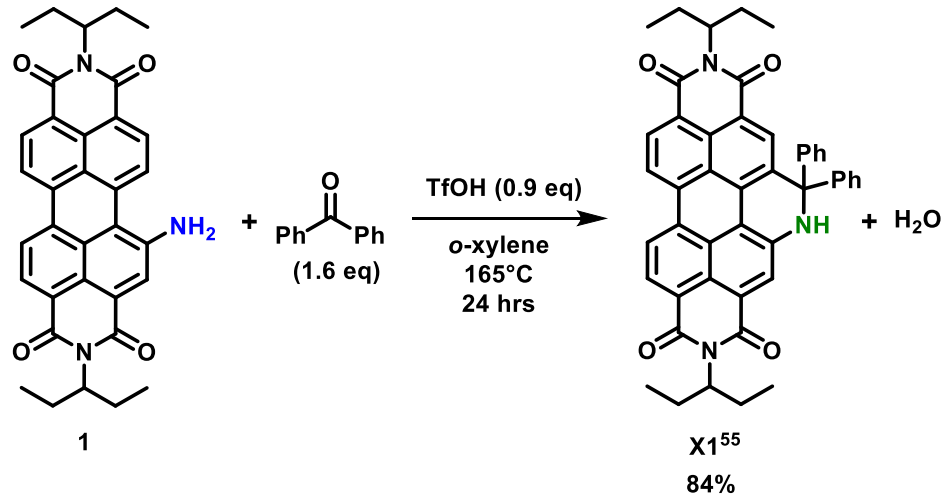

Figure 5: Synthesis of **X1**

our case we are installing a non-conjugated unit to the PDI core, whereas azabenz-annulated PDIs are fully conjugated. This creates an extra energy demand for our reaction, leading to the hypothesis that a stronger acid than TFA is needed in order to catalyze the reaction.

Before trying stronger Brønsted acids than TFA, we sought to probe the viability of catalyzing the reaction with a Lewis acid. The use of a Lewis acid catalyst to facilitate an amine condensation with a ketone was previously reported by the Bazan lab.[56] Entries 3 and 4 display the results for Tris(pentafluorophenyl)borane (BCF) and $TiCl_4$ Lewis acid catalysts. Attempts to use Lewis acid catalysis were unsuccessful, so we aimed to change the nature of our catalyst. Entry 5 displays the result for *p*-Toluenesulfonic acid monohydrate ($TsOH \bullet H_2O$) as no reaction, indicating that an even stronger acid is needed. Ohwada and co-workers reported a superacid catalyzed cyclization of an imine[57], leading us to believe that Trifluoromethanesulfonic acid (TfOH) may be able to catalyze the condensation and cyclization in a single step. Once TfOH was tried as the catalyst (Entries 6-

Table 1: Optimization of the synthesis of **X1**

Entry #	Catalyst	Catalyst eq.	Ketone eq.	Temperature (°C)	Time	Yield
1*	TFA	0.4	1.5	70	70 hrs	No reaction
2*	TFA	5.5	1.5	70	48 hrs	No reaction
3	BCF	1.5	1.5	70	18 hrs	No reaction
4	$TiCl_4$	1.5	1.5	70	18 hrs	No reaction
5	$TsOH \bullet H_2O$	3.0	1.5	70	24 hrs	No reaction
6	TfOH	1.5	1.2	165	24 hrs	11%
7	TfOH	1.5	1.0	165	24 hrs	8%
8	TfOH	1.5	1.5	165	24 hrs	33%
9	TfOH	0.9	1.6	165	24 hrs	84%

9) reactivity was observed. A yield of 84% was recorded and we felt the reaction had been adequately optimized at this point.

2.2. Reaction Mechanism

Figure 6 shows the possible reaction mechanism for the synthesis of **X1**. The reaction begins with the protonation of benzophenone to form the corresponding oxocarbenium ion. This was considered when developing the order of addition for the reaction, as TfOH and benzophenone were added first in an attempt to pre-form this intermediate. Next the nucleophilic attack of amino-PDI occurs on the carbonyl carbon to affect the condensation reaction. After a proton transfer step, the formation of the iminium ion is seen along with the loss of water. Once the iminium ion is formed its carbocation resonance form is utilized in the cyclization reaction to form the product **X1**. This carbocation resonance form is proposed as a key intermediate due to the resultant shifting of the phenyl groups out of the plane of the page, allowing the cyclization to occur.

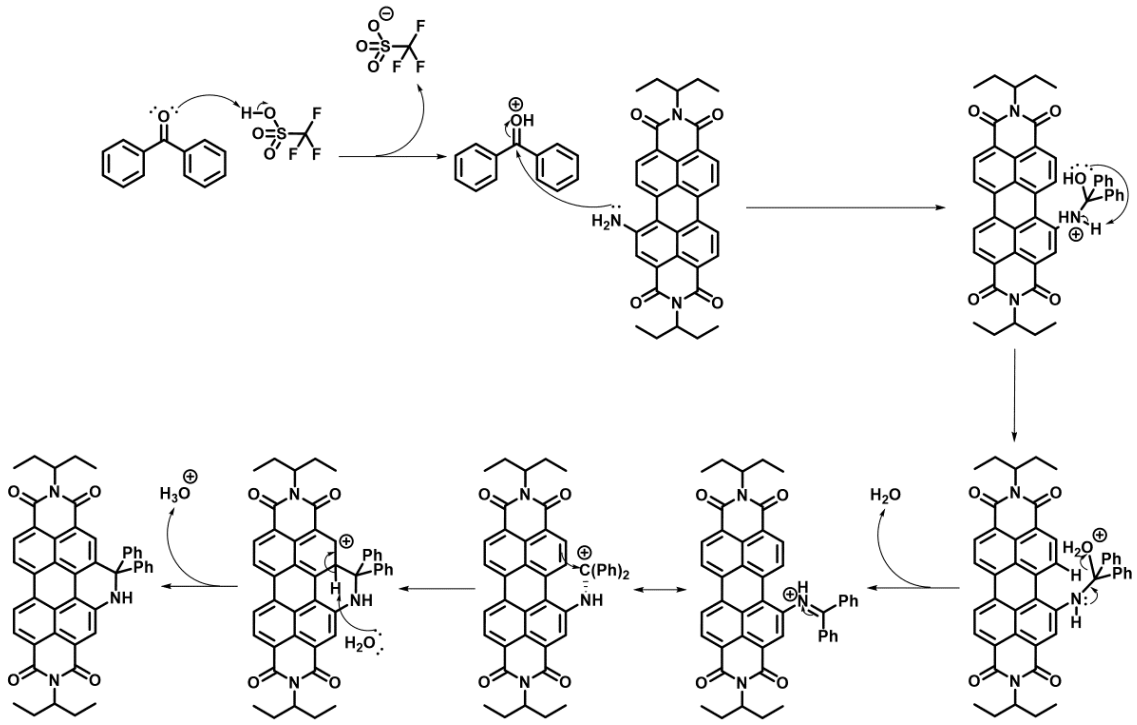

Figure 6: Possible Reaction Mechanism - Iminium ion intermediate

2.3. NMR Spectra of X1

Figure 7 shows the ^{1}H-NMR spectrum of **X1**. The most diagnostic peak in the spectrum is H_g and can be seen at ≈5.8 ppm which corresponds to the N-H proton present in the secondary cyclic amine. Integration of the aromatic peaks shows that there is a total of 6 aromatic hydrogens. This is further proof that the cyclization did occur because we would be expecting 7 aromatic hydrogens for the uncyclized imine product.

Figure 8 displays the DEPTQ-^{13}C-NMR spectrum of **X1**. The DEPTQ spectrum is a useful tool for assigning the peaks present in the standard ^{13}C-NMR spectrum. In the DEPTQ spectrum primary and tertiary carbon peaks appear in the downward direction while quaternary and secondary carbon peaks appear in the upward direction. The results of the ^{13}C-NMR spectrum peak

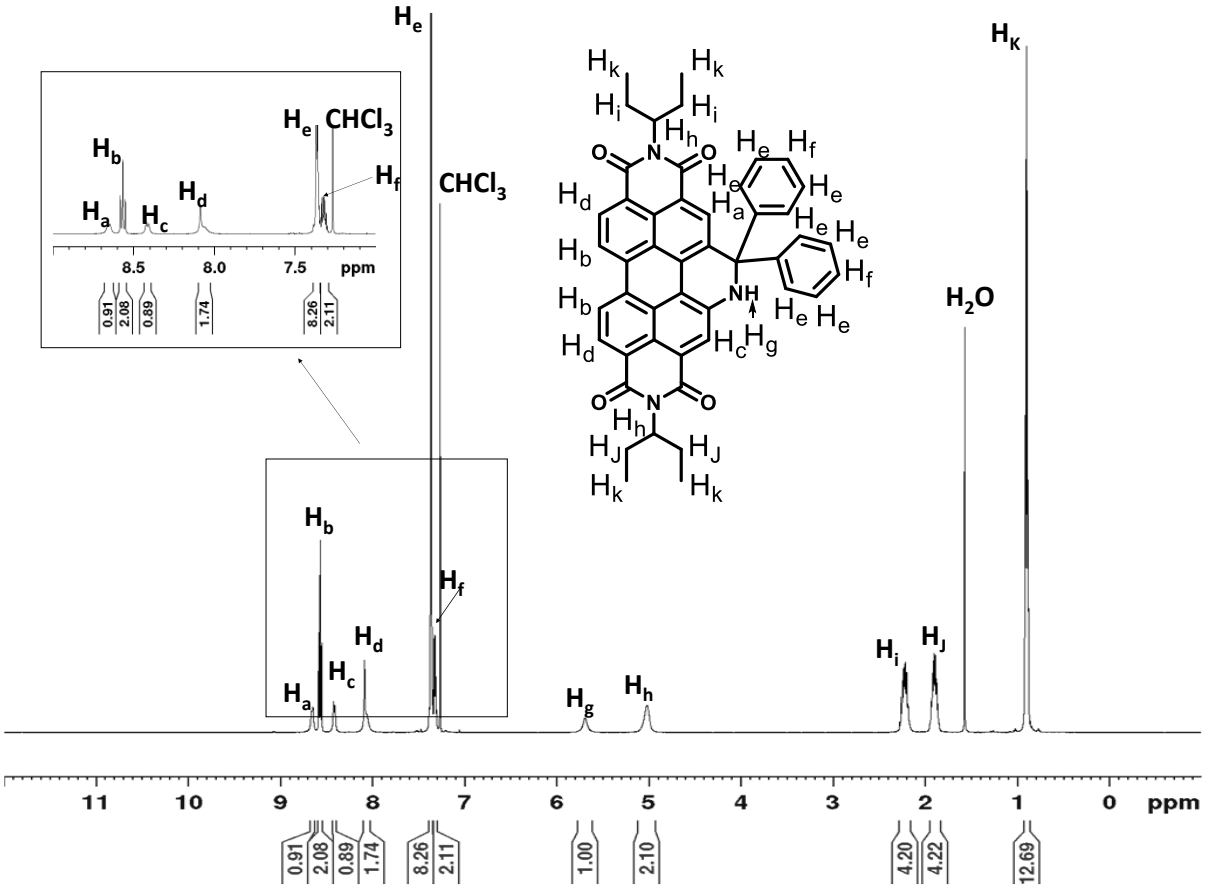

Figure 7: Assigned ^{1}H-NMR spectrum of **X1** in $CDCl_3$ recorded at 500 MHz

assignment can be seen in Figure 9. Quaternary carbons were unable to be distinguished from one another and were denoted with a Q.

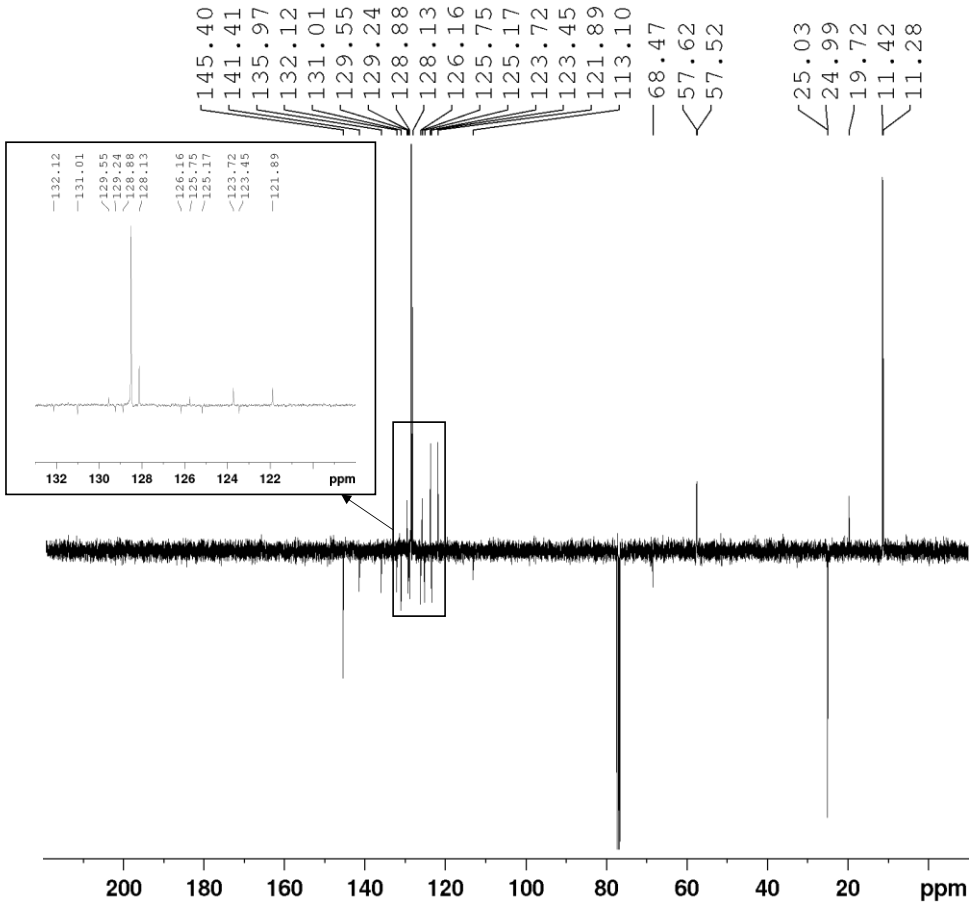

Figure 8: DEPTQ-^{13}C-NMR spectrum of **X1** in $CDCl_3$

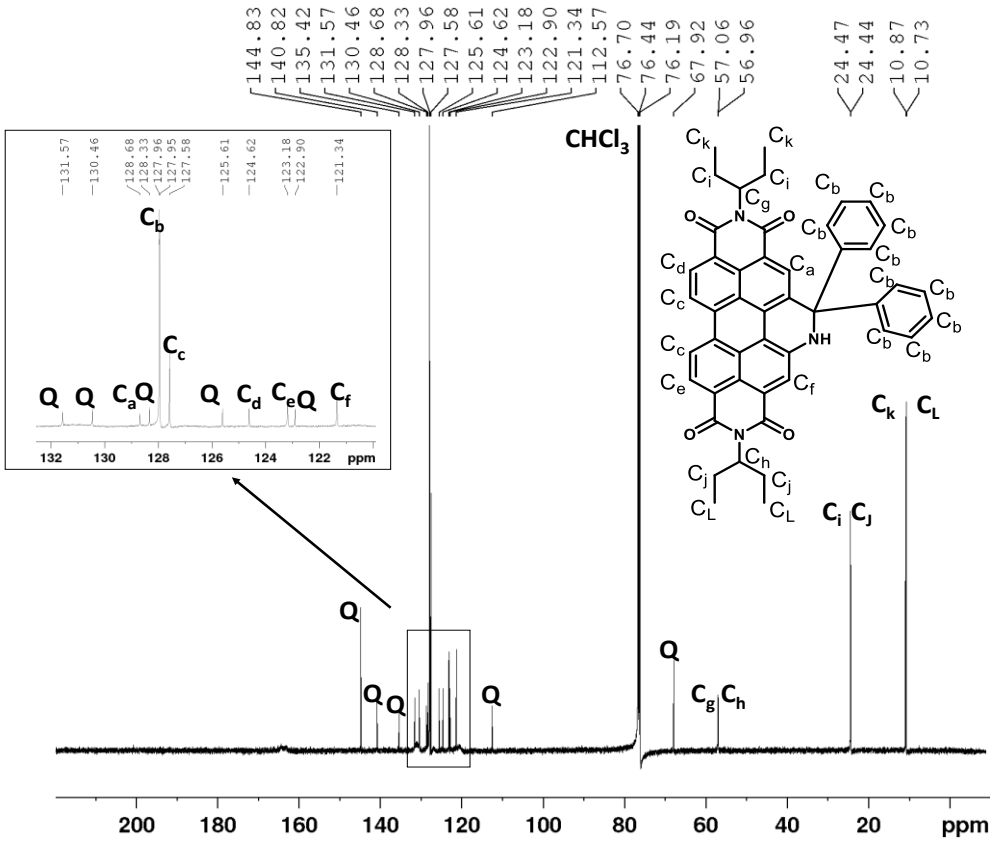

Figure 9: Assigned ^{13}C-NMR spectrum of **X1** in $CDCl_3$ recorded at 100 MHz

2.4. Optical Absorption Properties of X1

Optical Absorption results show that the secondary cyclic amine structure of **X1** causes it to have much different optical properties when compared to the parent PDI chromophore. Figure 10 shows the optical absorption spectra for **X1**, **1**, and PDI. The spectrum of **X1** displays what appear to be charge-transfer states[58] indicating that the vibronic coupling has been disrupted. Conversely, PDI shows strong vibronic coupling and a λ-max of 526 nm. The λ-max of **X1** is redshifted by

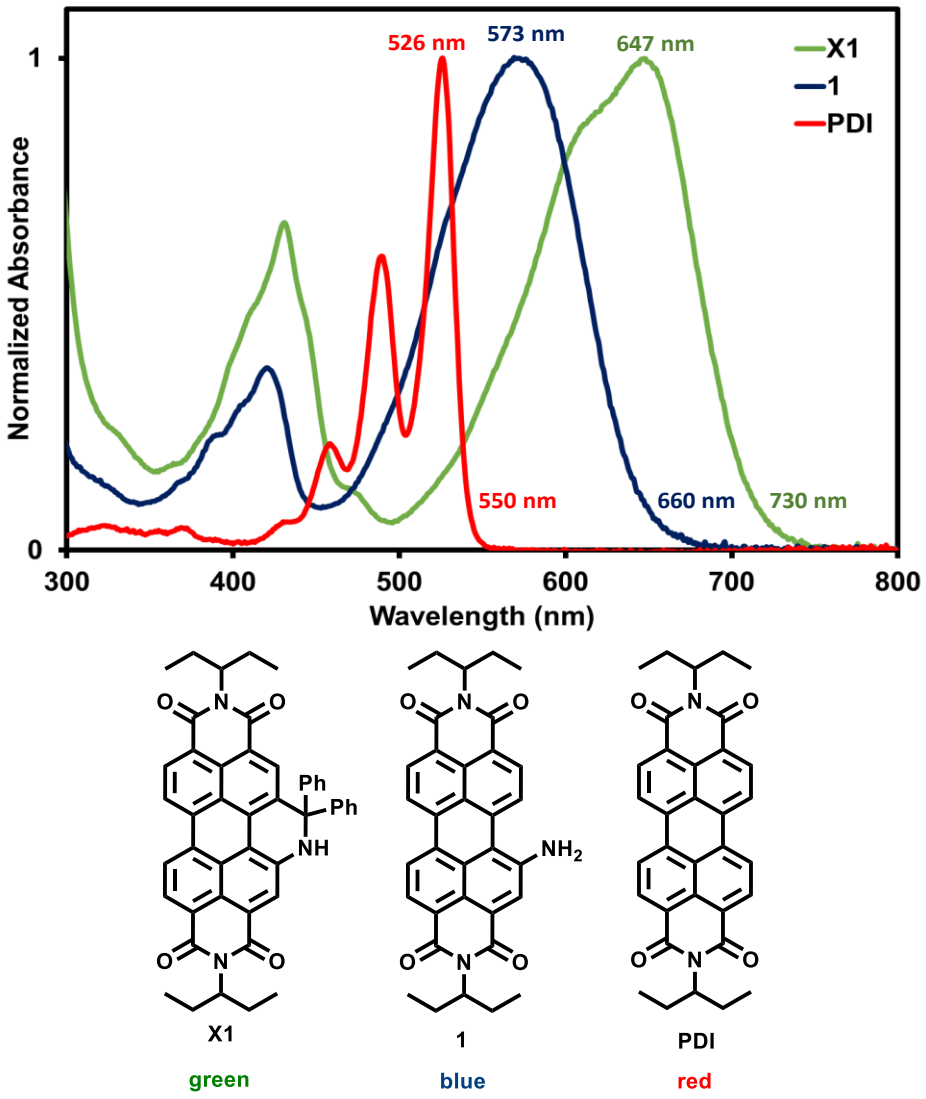

Figure 10: Optical Absorption Spectra of **X1**, **1**, and PDI recorded in $CHCl_3$ at room temperature

>100 nm when compared to PDI. The presence of a lone pair on the secondary cyclic amine contributes to the destabilization of **X1**'s HOMO, resulting in a destabilized π-system which leads to **X1**'s optical properties differing from PDI's.

When the spectrum of **X1** is compared to **1** there is much more subtle differences observed. Since **1** also has an amino lone-pair that can donate into the π-system we see a similar spectrum to **X1** but with a different λ-max at 573 nm. The major difference between **X1** and **1** is that for **X1** its amino lone-pair is fixed in position as it is part of a cyclic structure, leading to a less destabilized LUMO than **1,** and a smaller energy gap.

2.5. Electrochemical Properties of X1

For charge transport applications the determination of electronic energy levels is important. The electrochemical properties of **X1** were determined using cyclic voltammetry (CV, Fig. 11) with redox potentials confirmed via differential pulse voltammetry (DPV, Fig. 12). **X1** can be reversibly reduced twice, with $E_{1/2}$ values of -1.22 and -1.43 V, and reversibly oxidized once with $E_{1/2}$ of 0.62 V. The reduction behaviour is typical of PDI compounds, with $E_{1/2}$ values at higher

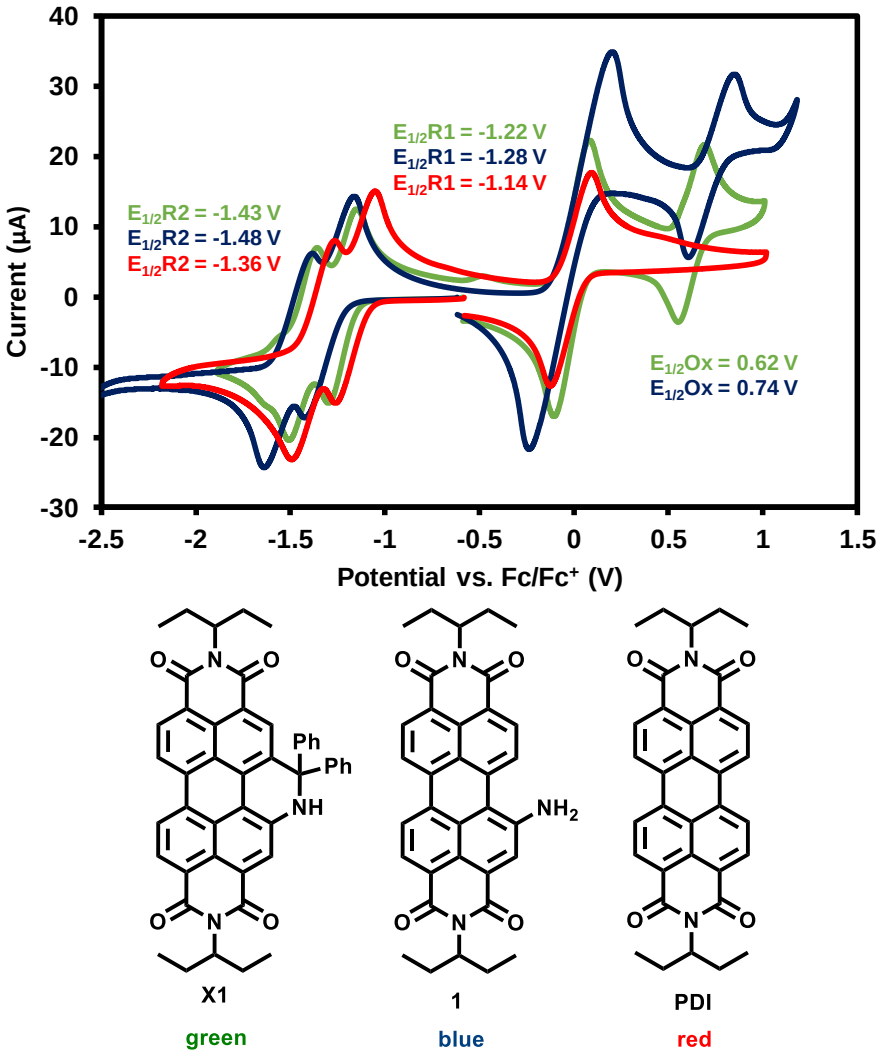

Figure 11: Cyclic Voltammogram of **X1** (green, ≈1 mM), **1** (blue, ≈1 mM), and **PDI** (red, ≈1 mM), in CH_2Cl_2, recorded at 100 mV/s. Half potentials listed.

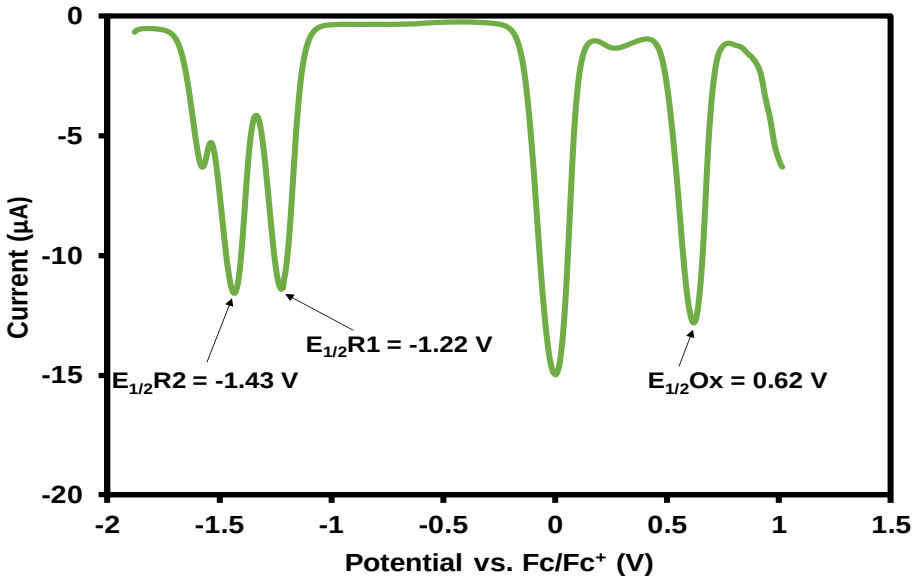

Figure 12: Differential Pulse Voltammogram of **X1** (≈1 mM) in CH_2Cl_2, recorded at 100 mV/s

potentials, owing to the cyclic secondary amine adding electron density to the system. Reversible oxidation is unique for PDIs, and in this case it is attributed to the presence of an electron rich nitrogen atom, consistent with that observed for **1** and the N-annulated PDI.[28-31] **X1** has a higher reduction potential than PDI (Fig. 11) which is consistent with the lone pair on nitrogen being able to donate electron density into the π* orbitals making the PDI harder to reduce. In comparison to **1**, **X1** has a lower reduction potential (Fig. 11) which suggests that the cyclic amine does not alter the electron affinity of the PDI chromophore as drastically as a primary amine substituent in the bay position. The redox potentials of **X1** determined by CV were confirmed *via* Differential Pulse Calorimetry (DPV, Fig. 12).

2.6. Processing and Solubility Characteristics of X1

In order to investigate the processing solvent options for **X1** the solubility of **X1** was tested on a 5 mg/mL scale to determine whether film formation was viable from each solvent. A concentration of 5 mg/mL was chosen because most solution processing techniques require a minimal concentration of 5 mg/mL to form a thin-film with thickness 20-100 nm, suitable for use in organic electronic devices. **X1** was soluble in chloroform, 2-methyl THF, *o*-xylene, ethyl acetate, and *n*-propanol:*n*-butylamine (1:1 v/v). The reason that the *n*-propanol:*n*-butylamine solution was chosen is that our lab has had success using alcohol/amine solutions to process PDI materials containing an N-H bond.[45] Thin-films were spin-cast from these solutions and pictures of the films can be seen in Figure 13. The films in Figure 13 were all formed successfully in a uniform manner. More experiments, such as atomic force microscopy (AFM) or polarized optical microscopy (POM), are needed to quantify the roughness of these films however upon visual inspection uniformity is observed. The results in Figure 13 provide a proof-of-concept that thin-films can be made from **X1** using eco-friendly solvents, furthermore they provide evidence that **X1** could be processed from an alcohol/amine solvent system. **X1** was not soluble up to 5 mg/mL in *n*-propanol alone, it required the addition of one volumetric equivalent of *n*-butylamine to be solubilized in *n*-propanol.

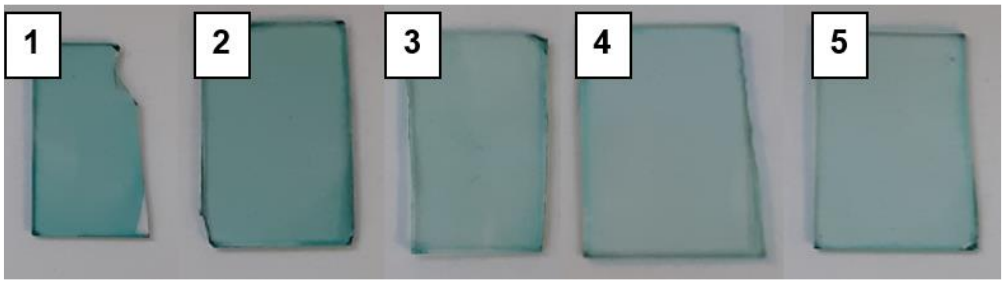

Figure 13: Pictures of thin-films of **X1** spin-cast from 5 mg/mL solutions onto glass substrate. (1) $CHCl_3$; (2) 2-Methyl THF; (3) *o*-xylene (4) EtOAc; (5) *n*-PrOH / *n*-butylamine (1:1 v/v).

The requirement of *n*-butylamine to solubilize **X1** in *n*-propanol prompted us to question whether it is necessary to have an acidic proton on the PDI molecule for dissolution to occur. In order to test this, a series of solutions of **X1**, **1**, and PDI were prepared that either contained only *n*-propanol as a solvent or contained a 1:1 v/v mixture of *n*-butylamine:*n*-propanol as the solvent. The results of this experiment are shown in Figure 14. It can be seen that **1** was soluble in 1:1 v/v *n*-butylamine:*n*-propanol and **X1** was soluble in 1:1 v/v *n*-butylamine:*n*-propanol, all other solutions were insoluble as precipitate was observed in solution. Since PDI was not soluble in *n*-propanol or 1:1 v/v *n*-butylamine:*n*-propanol, these results suggest that it is important to have an acidic proton available on the PDI molecule. These results verify the processing mechanism shown previously in Figure 3. The presence of an amine is necessary to solubilize **X1** in *n*-propanol. This supports the claim that base-promoted polarization of the N-H bond is occurring and consequently increasing solubility.

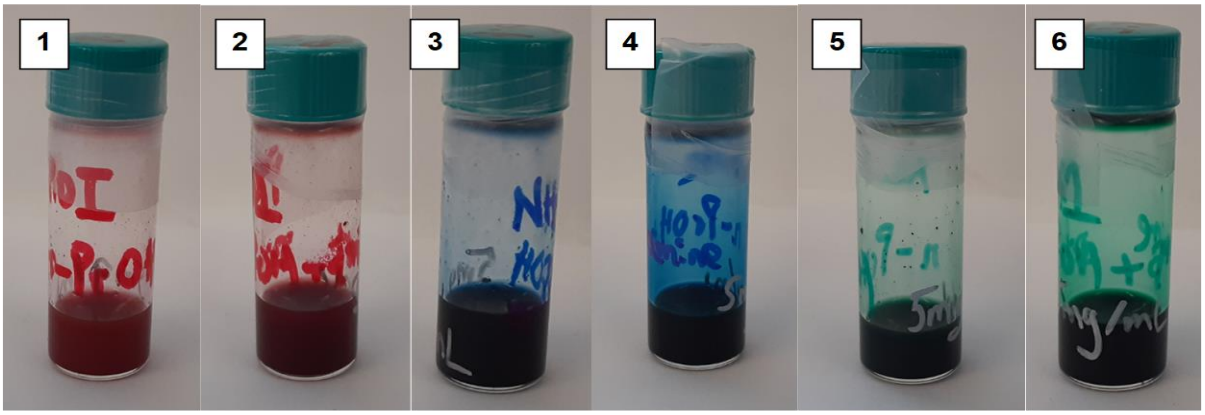

Figure 14: Pictures of 5 mg/mL solutions of: **PDI** (1) *n*-propanol and (2) *n*-propanol / *n*-butylamine (1/1 v/v). **1** (3) *n*-propanol and (4) *n*-propanol / butylamine (1:1 v/v). **X1** (5) *n*-propanol and (6) n-propanol / *n*-butylamine (1/1 v/v). All compounds could not be fully dissolved (up to 5 mg/mL) in *n*-propanol alone as seen with the particles on the vial sides. Note: compound **1** = PDI-NH_2

2.7. Thermal Properties of X1

Figure 15 shows the results for the thermogravimetric analysis (TGA) experiment of **X1.** The decomposition of **X1** started to begin at 360°C which while high, is lower than that for related N-annulated PDI (ca. >400°C)[29] suggesting the 6-membered ring is less stable than the 5-membered ring. Figure 16 displays the results for the differential scanning calorimetry experiment (DSC) of

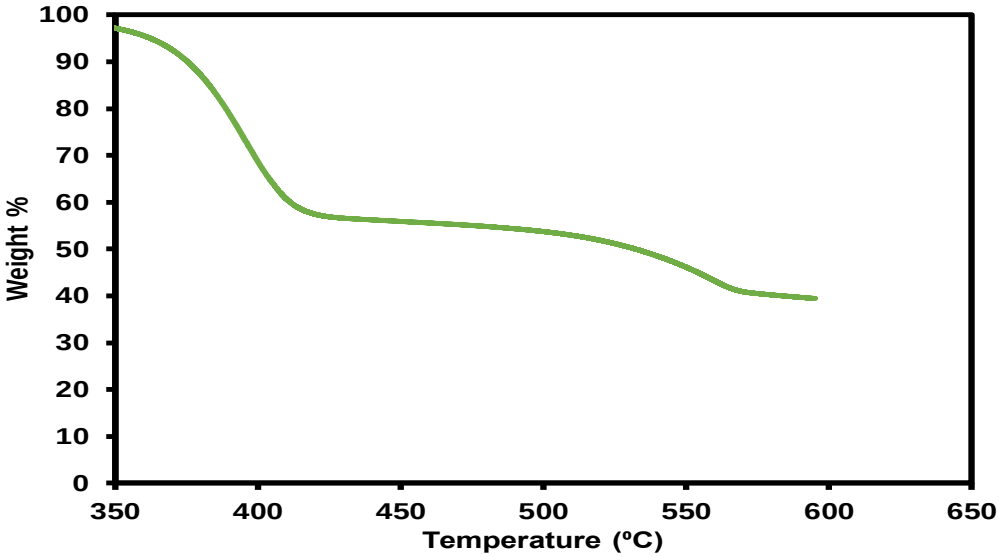

Figure 15: Thermogravimetric Analysis Experiment Results for **X1 –** Temperature vs. Weight% Plot shown

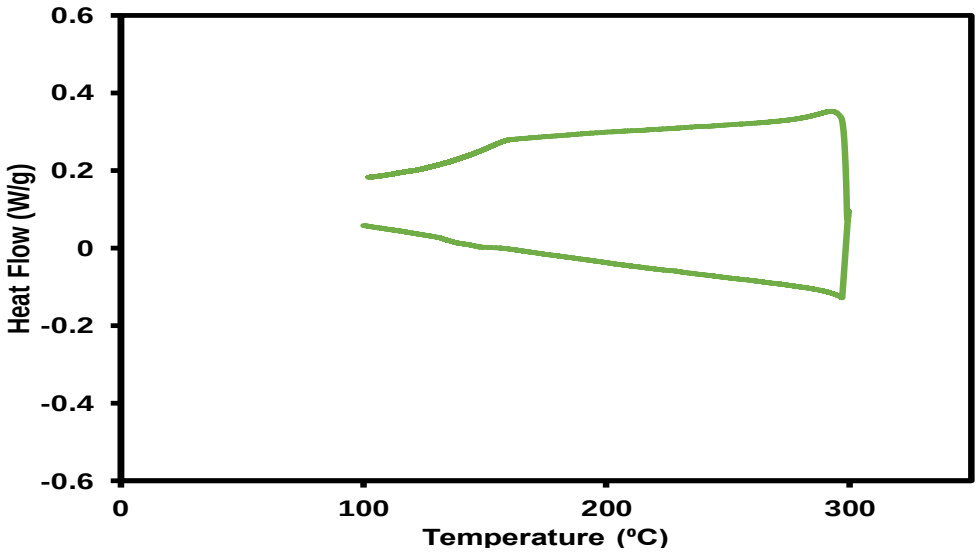

Figure 16: Differential Scanning Calorimetry Experiment Results for **X1 –** Temperature vs. Heat Flow Plot shown

X1. Large changes in heat flow are indicated by sharp peaks or spikes in a DSC experiment. These large changes can indicate the presence of glass transition temperatures, melting, evaporation, and crystalline states. In Figure 16 we only observe one large change in heat flow at ≈300 °C which is simply the melting of **X1**. In the case of **X1** there is not much information gained from this experiment other than providing the melting point of the compound.

2.8. Single Crystal Structure of X1

Single crystals of **X1** were grown using liquid-liquid diffusion of hexanes (1 mL) into a solution of **X1** (≈10^{-5}) in *o*-xylene (1 mL) at room temperature. Single Crystal X-Ray Diffraction (SC-XRD) confirms the cyclic secondary amine structure of **X1** due to the presence of a non-planar nitrogen atom within the newly extended ring system. The single crystal structure of **X1** (Fig. 17) exhibits a slightly bowed PDI core. The two phenyl groups are orientated above and below the PDI core and do not impede the formation of a one dimension NH••O=C hydrogen bonded network in **X1** (N..O = 3.0190(17) Å), though π- π interactions are limited to a single adjacent molecule (ring centroid-centroid = 3.6904(1) Å). This data was collected and solved by Benjamin S. Gelfand.

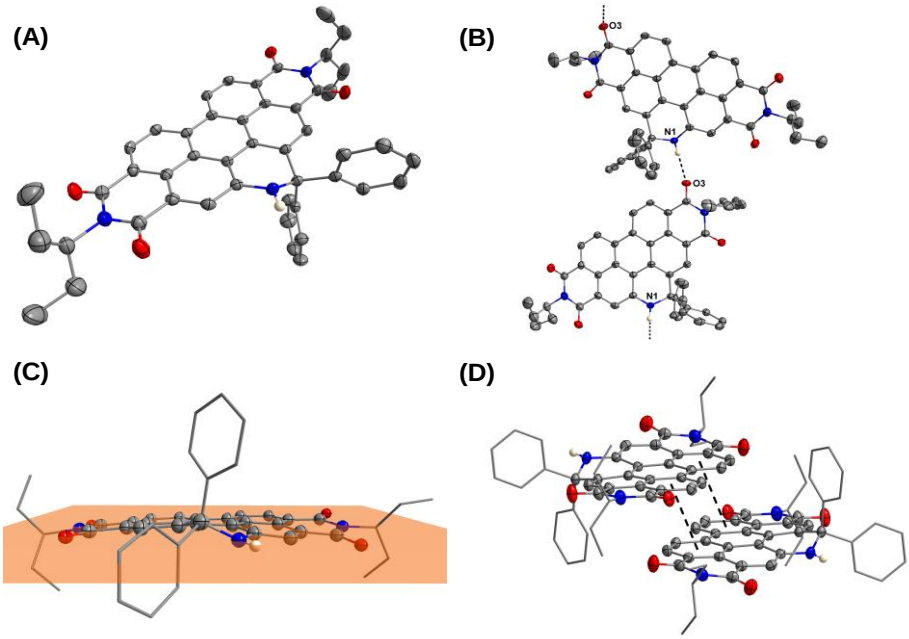

Figure 17: Structural features of **X1** (A); including: (B) H-bonding network; (C) the mean plane through the PDI core, excluding the annulated cyclic amine, indicating the bowed nature of the core; and (D) π-π stacking pairs present in **X1.** C, H, N, O are grey, cream, blue, and red, respectively. Ellipsoids and H atoms are represented at 50% probability and 0.2 Å, respectively. H atoms bonded to C atoms, the minor disorder component, and solvent molecules have been omitted for clarity. In (B) and (C), H-bonds and ring centroid-centroid interactions are shown by black dashed lines. In (C) and (D), the imide and annulated side chains are represented by wires for clarity.

2.9. Organic Field Effect Transistors

The following work was performed by our collaborators Samantha Brixi and Benoit H. Lessard as part of the NSERC Strategic Network Grant – Green Electronics Network.

Proof of concept OFET devices were fabricated using **X1** in bottom gate, bottom contact configuration. **X1** films were formed by spin-coating of n:propanol:*n*-butylamine (1:1, 5mg/mL) solutions. Isopropanol was compared to *n*-propanol as different vapour pressure can give slightly different films. Devices were thermally annealed for 1 hour under vacuum at either 70, 150, or 200 °C. Consistently, annealing at a higher temperature improves device mobility at low channel length, but only confers modest improvement at higher channel length (Fig. 18 and 19). The threshold voltage (*VT*) has exceptional improvement at higher channel length, with notable but smaller improvements at lower channel length. Electron mobilities up to mid-10^{-5} cm^2 V^{-1} s^{-1} at a channel length of 2.5 µm, and 10^{-5} cm^2 V^{-1} s^{-1} at 20 µm channel lengths were observed. Annealing was necessary to drive away residual amine which can act as charge traps. The *VT* of approximately 10 V, when annealed at 200 °C, is promising for an n-type material. It is particularly encouraging, as we have demonstrated that the *VT* is tuneable through processing conditions and this could be further improved with simple contact engineering.[59] While the electron mobility values are not near that of the top performing PDI based OFETs[17-19] (ca. 0.1-0.5 cm^2 V^{-1} s^{-1}) and

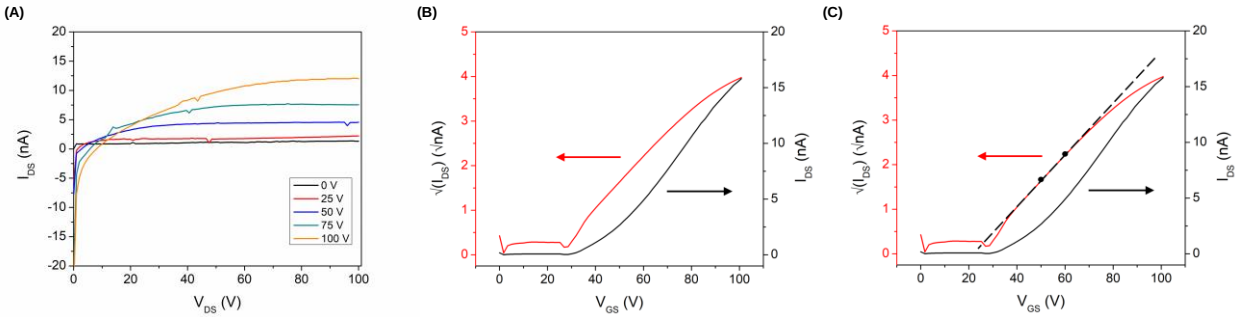

Figure 18: Example OFET output plots (a), transfer plots (b), and transfer plots showing linear region (c) for devices based on films of **X1** processed from *n*-propanol:*n*-butylamine (1:1) solutions and annealed at 200°C.

devices are not air stable, **X1** itself is air stable and active layers were processed from alcohol-based solutions which is rare.

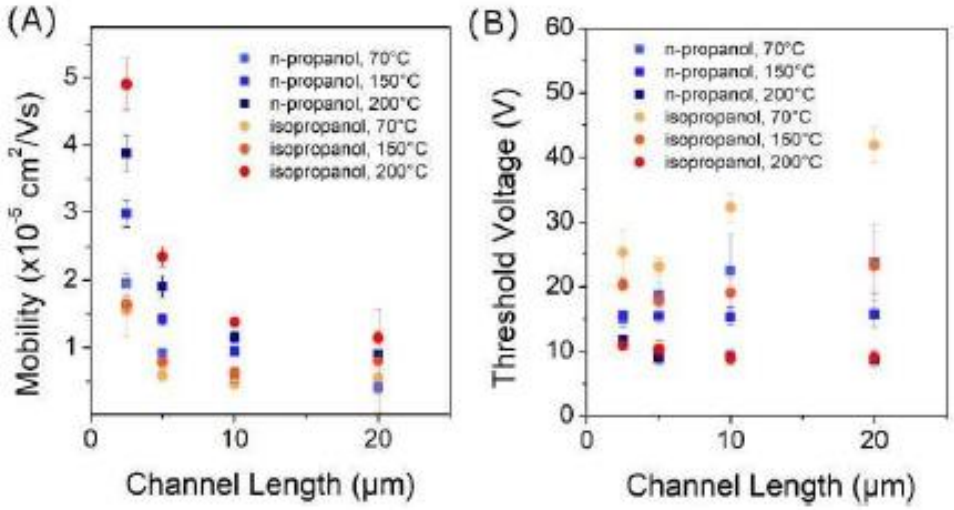

Figure 19: A) Electron mobility and B) threshold voltage of OFET devices based on **X1** films cast from *n*-propanol:*n*-butylamine (1:1) solutions and annealed from 70-200 °C

3. Electronic Structure and Design of New Targets

3.1. Design of New Target Molecules

A major criticism of **X1** was that it did not have a high enough electron affinity to be a high performing n-type material in OFETs. Increasing the electron affinity will allow for: 1 – Lowering of the LUMO energy level for sufficient alignment with the work function of the electrodes. The work function of common electrodes such as aluminum, silver, and gold ranges from -4 to -5 eV.[60] Thus lowering the LUMO energy level from ≈-3.6 eV closer to -4 eV allows for better electron transfer; 2- Increase air-stability to prevent electron transfer to O_2 and subsequent superoxide formation.

With our newly developed synthetic method in hand, we sought to design and synthesize a new series of targets which could be a top performing material. Major questions at this point included: 1 – Will the synthetic method be robust enough to apply to other types of ketones? 2 – Where can electron withdrawing groups be placed in order to maximize their effect on the electron affinity?

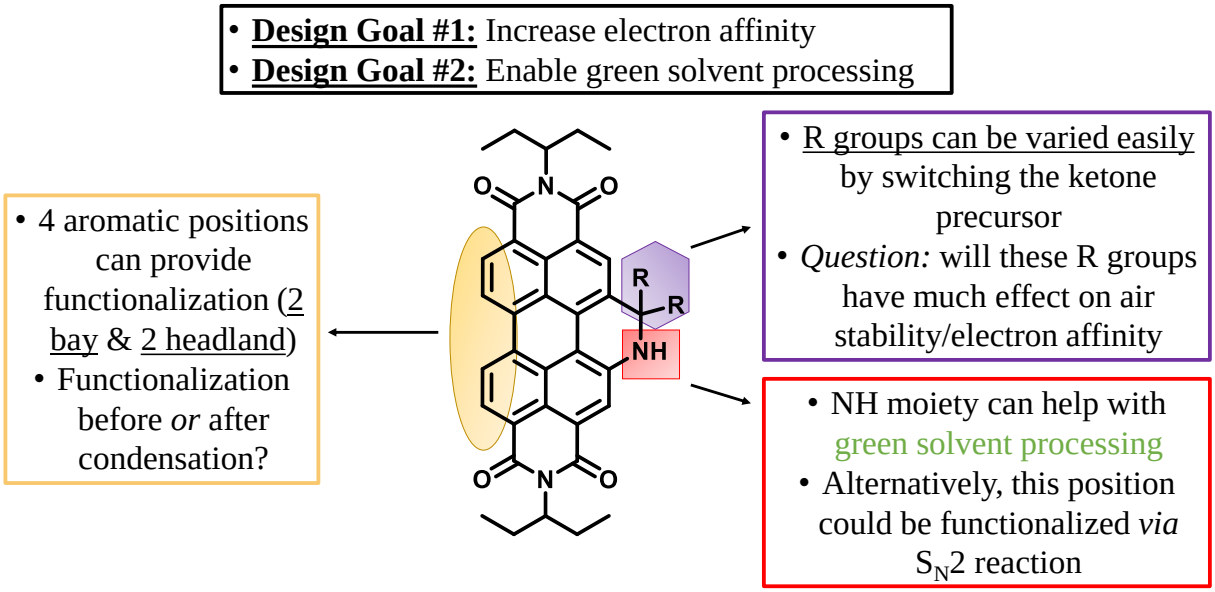

Figure 20: Molecular design considerations for future targets bearing the 6-membered cyclic amine seen in **X1**.

3 – How will these electron withdrawing substituents affect processing and green solvent solubility characteristics? Keeping these points in mind we began to envision what our new synthetic targets might look like. Figure 20 shows our two major design goals which are to increase electron affinity and to keep the same green processing that we saw previously with **X1**. There are a variety of options for synthetic derivatization within this new molecular framework. Classical aromatic substitution reactions can be performed on the opposite bay position(s). Additionally, the imide and R groups of the ketone precursor can be synthetically varied to tune the optoelectronic properties of our final target. Historically, PDIs are known for exhibiting drastic changes in optoelectronic behaviour when the bay position(s) is substituted. This was seen earlier in the compound **1** which is blue in colour while its analogous non-substituted PDI is red. In comparison, we are unsure how much of an effect the R groups of the ketone precursor have on the overall electron affinity. Due to the location of the R groups within the molecule I would speculate that inserting electron withdrawing groups at this position will have a less drastic effect as the opposite bay position. This is due to the absence of conjugation with respect to the R groups. However, it is impossible to say at this point whether this is true or not because these molecules have never been synthesized before. It will be exciting to see how the substitution of each position will affect the properties of these materials, once synthesis is complete.

3.2. New Synthetic Targets

Figure 21 shows the new series of compounds that we aim to synthesize. The targets shown were chosen to maximize overall performance and to also gain insight on how broadly the reaction methodology from the **X1** paper can be applied. The latter point is illustrated in target **2** which does not address our design goal to increase electron affinity, however if the synthesis is successful then various alkyl ketone derivatives bearing electron withdrawing groups could be utilized in hopes of synthesizing a high performing n-type organic semiconductor (OSC). In the case of **X2** it is advantageous to synthesize this product containing aryl bromide substituents as the aryl bromide derivative allows for further functionalization *via* palladium catalyzed cross-coupling reactions.[61-63] Overall, the targets shown in Figure 21 will provide a nice comparison between the placement of electron withdrawing groups within the molecule and the overall performance once the project is completed. Similar to the **X1** project, we will collaborate with Benoit Lessard's laboratory for OFET device data on successfully synthesized targets.

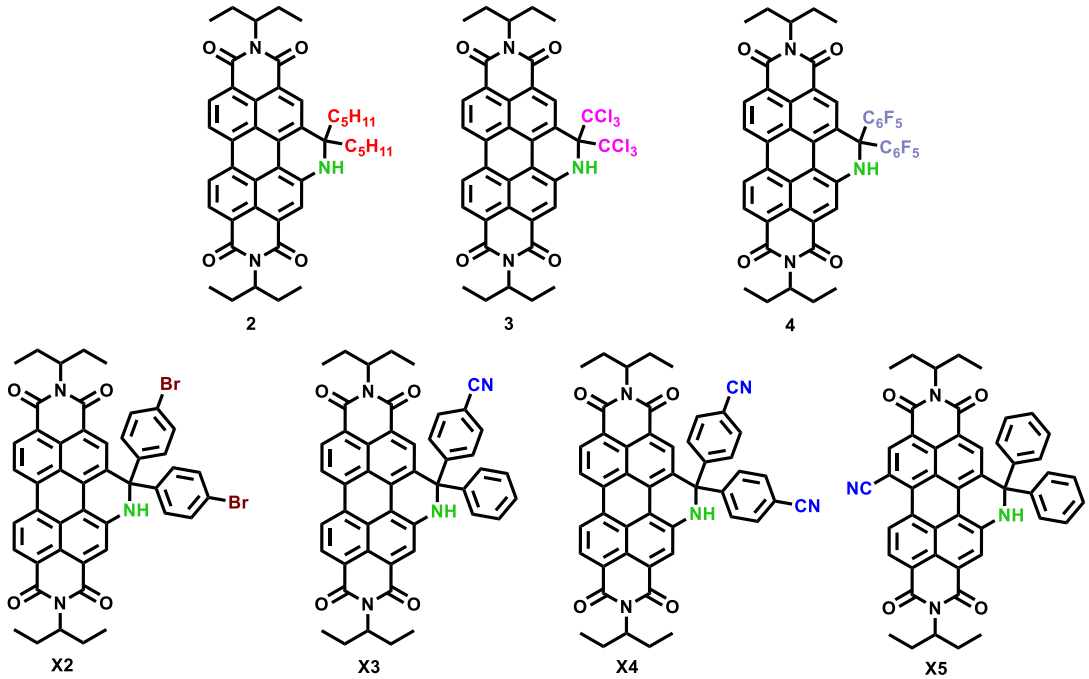

Figure 21: Defining new synthetic targets accessed *via* acid-catalyzed condensation: **2, 3, 4, X2, X3, X4**.

3.3. DFT Electronic Structure Analysis

In a hope to understand the electronics of our future synthetic targets at a higher level we decided to take advantage of our lab's collaboration with the Rondeau-Gagné lab located at the university of Windsor *via* GreEN. Their ability to perform density functional theory (DFT) calculations and provide energy level diagrams of potential materials were skills that we wished to utilize in the analysis of our new molecular framework. This gave us the opportunity to investigate how the placement of new electron withdrawing substituents will affect the overall electronics of the target molecule. Figure 22 shows the DFT energy levels generated by our

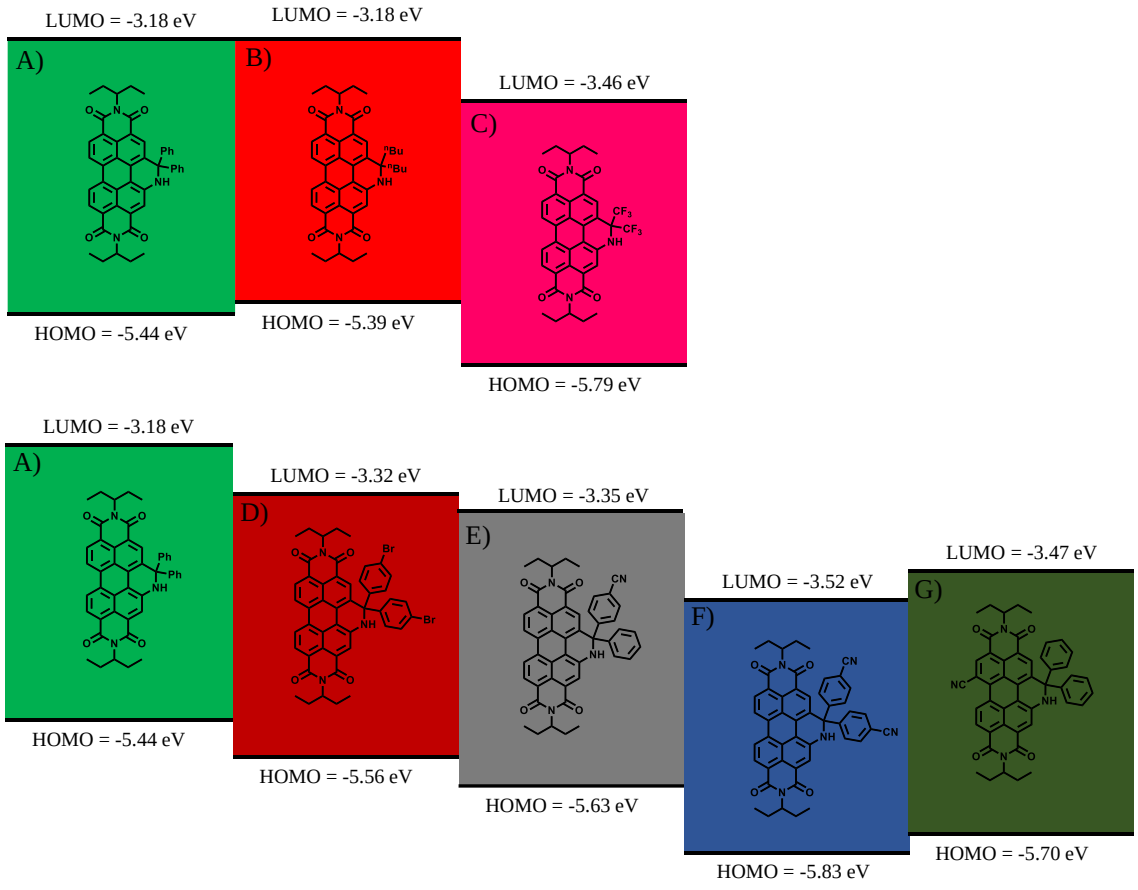

Figure 22: DFT energy level diagrams for: A) **X1**, B) **1a**, C) **2a**, D) **X2**, E) **X3**, F) **X4**, G) **X5**

collaborators Michael Ocheje and Simon Rondeau-Gagne. A lowering of the energy of the HOMO and LUMO energy levels is an indication that the electron affinity is increasing. **X1** has a LUMO energy level of -3.18 eV and HOMO energy level of -5.44 eV. Figure 22 shows that when the phenyl groups of **X1** are replaced with *n*-butyl groups (**2**, Fig 22) the LUMO energy level remains the same while the HOMO energy level is slightly higher than **X1**. This result is somewhat expected since there is not a major difference in electron withdrawing character between these two structures. Replacing the *n*-butyl groups (**2a,** Fig 22) with trifluoromethyl groups (**3a**, Fig 22) lowers the HOMO and LUMO energy levels to -3.46 eV and -5.79 eV respectively. These results indicate that introducing electron withdrawing substituents on the ketone precursor does increase the electron affinity. This validifies developing a synthetic strategy to access haloalkyl **X** derivatives as they may possess desirable device performance characteristics.

Figure 22 shows the HOMO and LUMO energy levels for **X2** are -3.32 eV and -5.60 eV. The LUMO and HOMO energy levels of **X3** and **X4** are lower than that of **X2** (Fig. 22) indicating that the substitution of the phenyl groups can lead to an increase in the electron affinity. Overall, it is shown that derivatization *via* varying the nature of the aryl ketone precursor can be an effective strategy to tailor electronic properties in our favour.

Figure 22 shows the DFT results for the **X5**. The LUMO and HOMO energy levels are -3.47 eV and -5.7 eV respectively. It is interesting that this molecule does not have lower LUMO and HOMO energy levels than **X4** discussed earlier, indicating that the substituents on the ketone precursor may have more of an effect on the electronic nature of the molecule than we had initially thought.

4. Synthesis of New X-Type Products

4.1. Alkyl Ketones

In order to understand possible applications our new synthetic methodology more, we aimed to expand the substrate scope. The viability of the reaction with alkyl ketones was tested first. Figure 23 shows the reaction of **1** with 6-udecanone and hexachloro-2-propanone under identical reaction conditions as the **X1** synthesis. The synthesis was unsuccessful in both cases. Referring to the reaction mechanism (Fig. 6) it can be seen that in order for the reaction to proceed an oxocarbenium ion must form from the ketone precursor before proceeding to the formation of the iminium ion intermediate. The reactions in Figure 23 involve ketone precursors which do not contain aryl substituents, as was the case with **X1**. This indicates that the formation of the initial

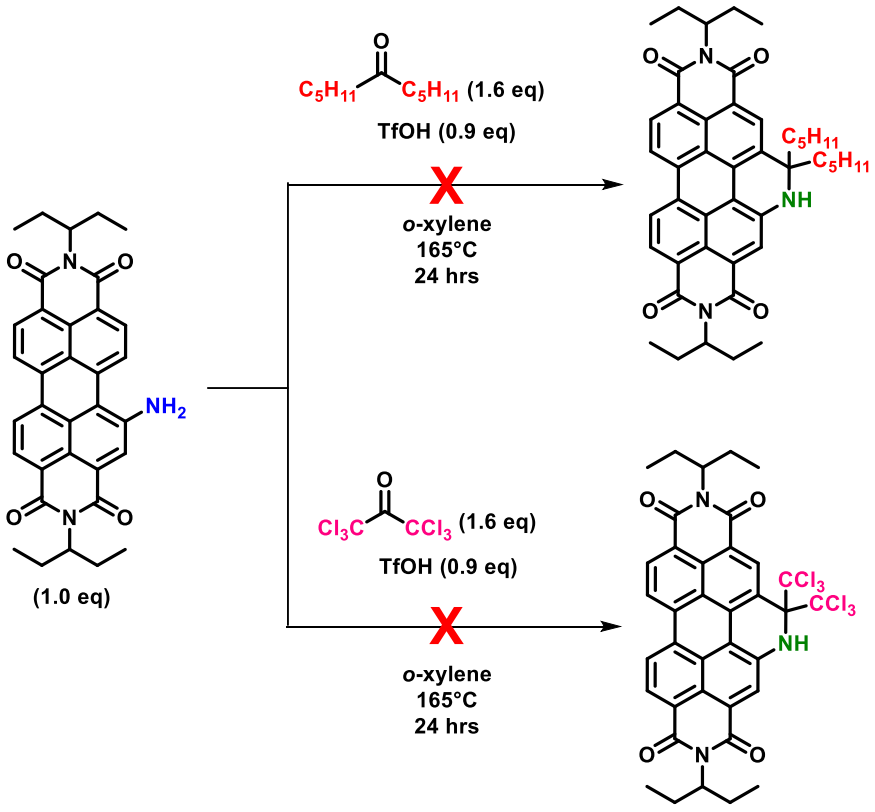

Figure 23: Attempted synthesis with alkyl and chloroalkyl ketone precursors

oxocarbenium ion is less favourable for the synthetic pathways shown in Figure 23. This is possibly a limitation to our newly developed synthetic methodology, however the reactions shown in Figure 23 have only been tried once under identical **X1** conditions. Speculation leads one to consider what the consequence of adding more acid catalyst to the reaction would be. It is possible that adding more acid can promote the formation of the oxocarbenium ion and drive the reaction forwards to completion. Figure 24 shows a comparison of the ^{1}H-NMR spectra for **1**, **X1**, **2**, and **3**. It is highlighted in the ^{1}H-NMR spectrum of **X1** where the characteristic N-H proton appears at ≈5.8 ppm. Inspection of the red and purple spectra shows that there is no peak present in this region of the spectrum which would correspond to the N-H in our final desired product. The spectrum of **1** shown in blue displays a slight overlap of two peaks at ≈5 ppm. Using this as an indicator when looking back at the two new reactions presented, we observe a very similar peak overlap at ≈5 ppm. This information is indicative that our starting material may not have been consumed in the reaction. These ^{1}H-NMR spectroscopic results suggest that the two new reactions under investigation did not go to completion, although some reactivity was observed.

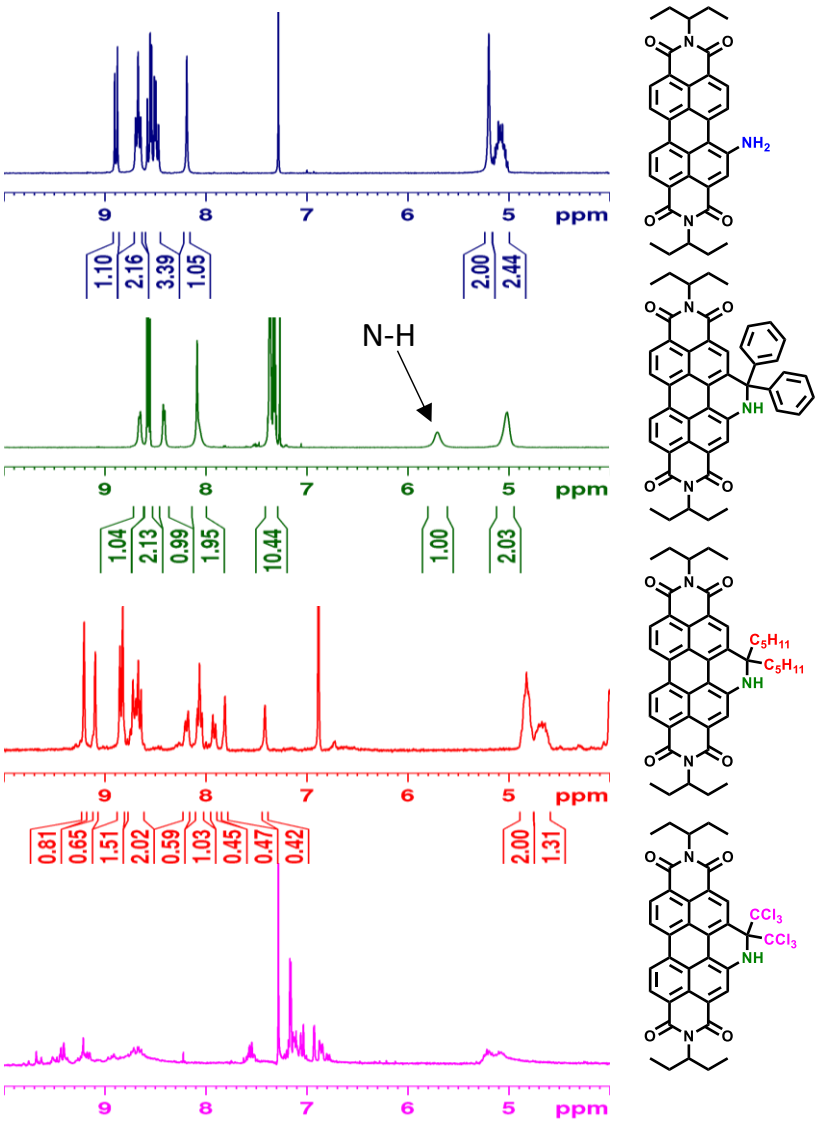

Figure 24: [1]H-NMR spectra stack-plot (10 to 4 ppm) of **1**, **X1**, and work-up NMR spectra of reactions conducted to access the two desired products shown

4.2.Substituted Aryl Ketones

Continuing with the goal of expanding the substrate scope of the reaction we turn our focus to substituted benzophenone derivatives. The design principles discussed previously still apply, as we are still trying to incorporate electron withdrawing groups into the final products to increase electron affinity. Extending the synthetic methodology to substituted benzophenones will help us further understand how electron withdrawing substituents effect the overall reaction.

Figure 25 shows the synthesis of **X2** and **X3** as well as the attempted reaction with decafluorobenzophenone. The reaction was successful in synthesizing the new targets **X2** and **X3** although the reaction unsuccessful with decafluorobenzophenone. These new results indicate that there may be a detrimental impact on the percent yield when electron withdrawing substituents are

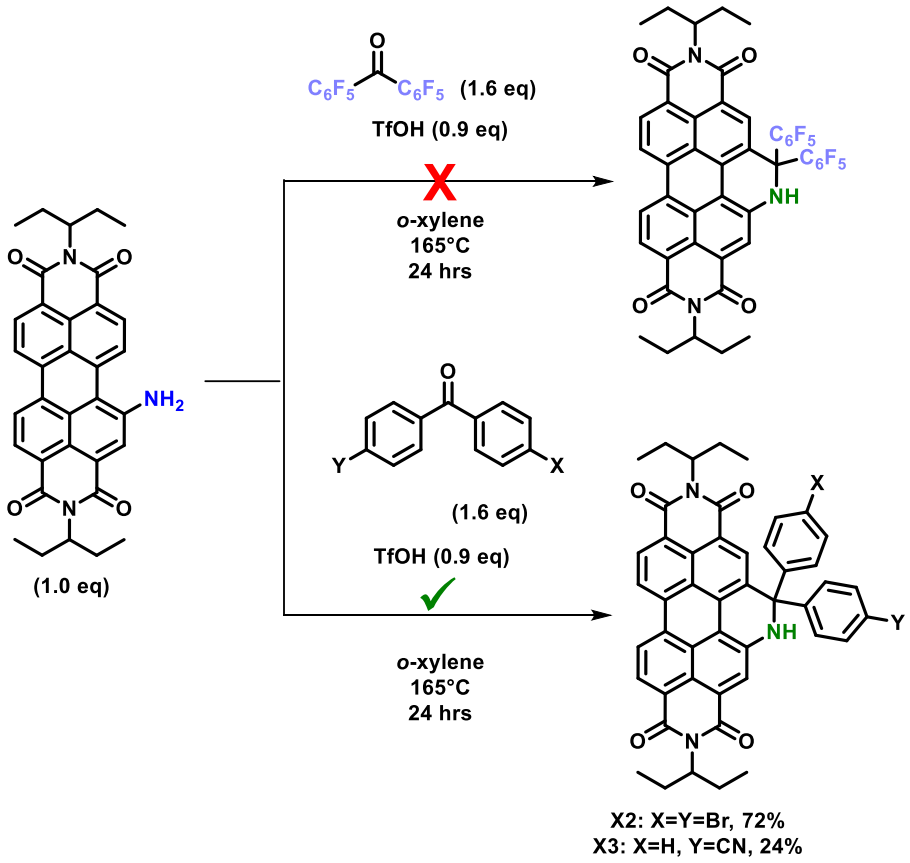

Figure 25: Synthesis of **X2** and **X3**

introduced. The impact of molecular electronics on the reaction becomes more interesting when a comparison is made between the yields of **X1**, **X2**, and **X3**. It appears that the yield of the reaction decreases when electron withdrawing groups are introduced. This can be seen when comparing **X1** (84%) to **X2** (72%), furthermore when the strongly electron withdrawing cyano group is present in **X3** the yield is only 24%, which is a 60% difference from the synthesis of **X1** under identical conditions. It is likely that by introducing electron withdrawing substituent(s) the oxocarbenium intermediate and the iminium ion previously shown in Figure 6 are destabilized which slows down the reaction. This clearly presents a problem as the goal of this project is to synthesize molecules which contain electron withdrawing groups. There is always a way to optimize any reaction and again speculation leads one to consider whether more equivalents of the TfOH catalyst may be the key to help increase the yield of **X3**.

Figure 26 shows the ^{1}H-NMR spectrum of **X2**. The diagnostic N-H peak appears at ≈5.6 ppm once again, indicating that the introduction of bromo substituents at the *para* positions does not have a large impact on the chemical shift as it is about the same as the N-H chemical shift for **X1**. In the case of **X2** the aromatic hydrogens from the ketone precursor are resolved into two sets of peaks due to the influence of the bromo substituents. Integration gives 4 protons each for the *ortho*

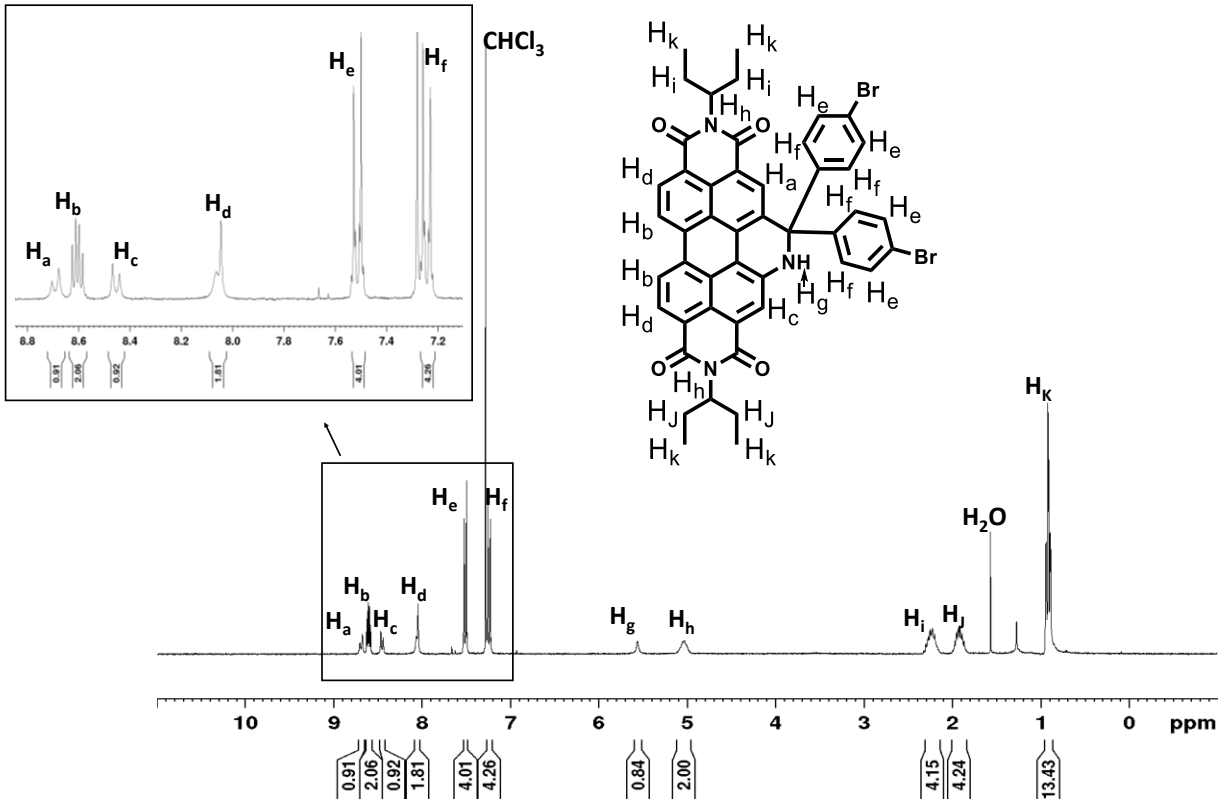

Figure 26: ^{1}H-NMR spectrum of **X2** in $CDCl_3$ recorded at 300 MHz

and *meta* positions. Once again, the peaks for the hydrogens labelled H_d appear to be overlapped as was the case with **X1**. Figure A1-3 displays the mass spectrum for **X2**, and it is evident that the proposed structure was synthesized in the reaction.

Figure 27 displays the ^{1}H-NMR spectrum of **X3**. There are three separate sets of peaks for the aryl groups attributed to the ketone precursor labelled H_e, H_f, and H_g. The diagnostic N-H peak is labelled H_h and it appears at ≈5.9 ppm which is slightly further downfield than what was shown previously for **X1** and **X2**. It appears that the strong electron withdrawing nature of the cyano

group influences the chemical environment of the N-H proton. More experiments need to be done, but this is a sign that the N-H proton may be slightly more acidic in the case of **X3**.

Figure 28 shows the proposed synthesis of **X4**. This reaction has not been tried yet however our lab has had previous success using CuCN for these types of reactions. The cyanation of an aryl bromide with CuCN has been previously reported by Mukhopadhyay and coworkers on a PDI analogue.[64] In the event that this reaction is unsuccessful there are other options that could be explored such as in the Marks paper discussed earlier where they use zinc cyanide and a Pd^0

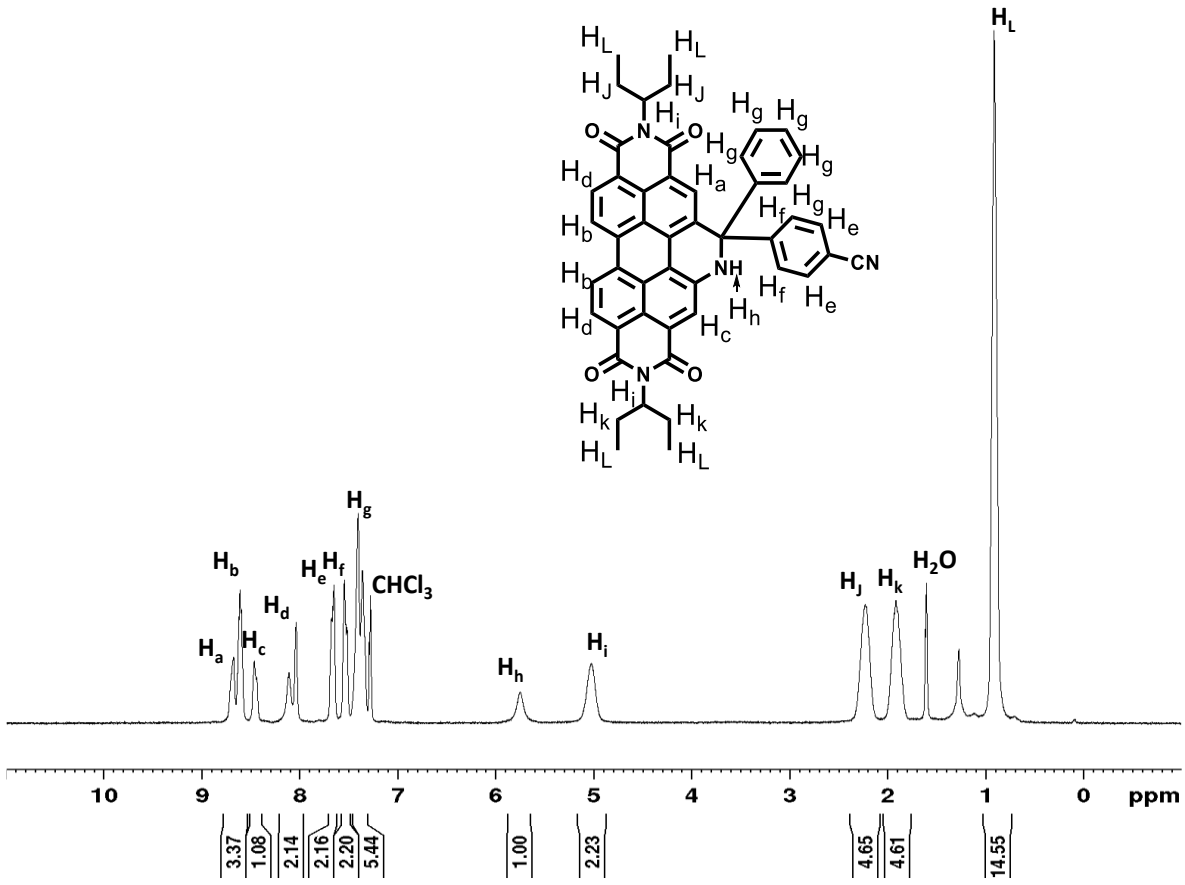

Figure 27: ^{1}H-NMR spectrum of **X3** in $CDCl_3$ recorded at 300 MHz.

source.[17-19] Nevertheless the introduction of two cyano groups on **X4** will make an interesting comparison with **X3** in terms of overall device performance and green solvent solubility.

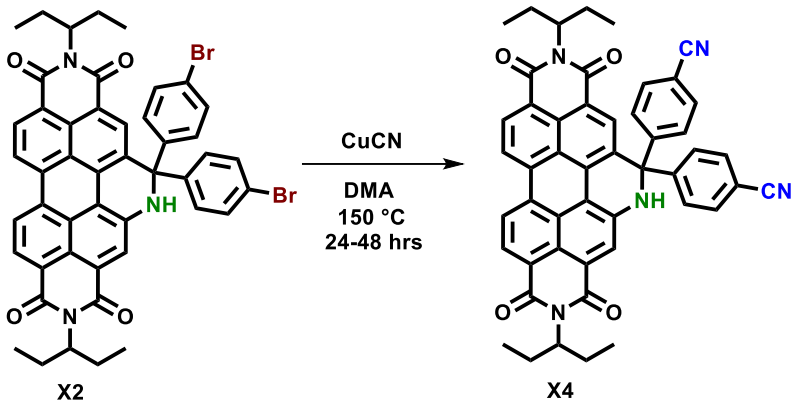

Figure 28: Proposed synthesis of **X4**

4.3. Functionalization of X1

The next synthetic path to explore involves the synthetic functionalization of **X1**. Our goal is to brominate **X1** at the opposite bay position in order to then convert the aryl bromide to a cyano group. While performing the initial bromination reaction an interesting discovery was made. Figure 29 shows the synthetic results of the bromination of **X1**. Rather than seeing the bromination occur selectively at the opposite bay position it occurred at the opposite bay position AND the headland position closest to the N-H moiety. This is confirmed by the ^{1}H-NMR spectrum (Fig. 30) and the HRMS Mass Spectrum (Fig. 31). Even though the synthesis of the desired product **5** was unsuccessful, this result is quite exciting. When **X6** is compared to the bis-cyano PDI discussed

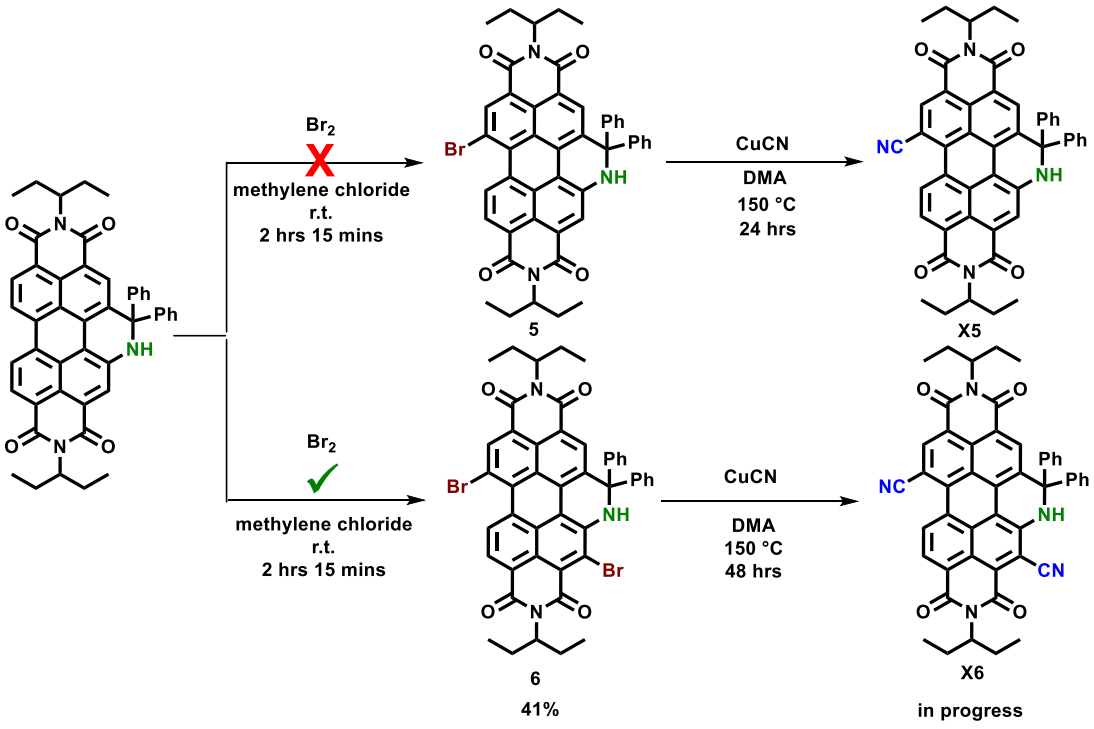

Figure 29: Synthetic results from the treatment of **X1** with liquid bromine.

previously, it is not unreasonable to say that **X6** could have the same high performance as the bis-cyano PDI and be green-solvent-processable due to the presence of the polarizable N-H bond.

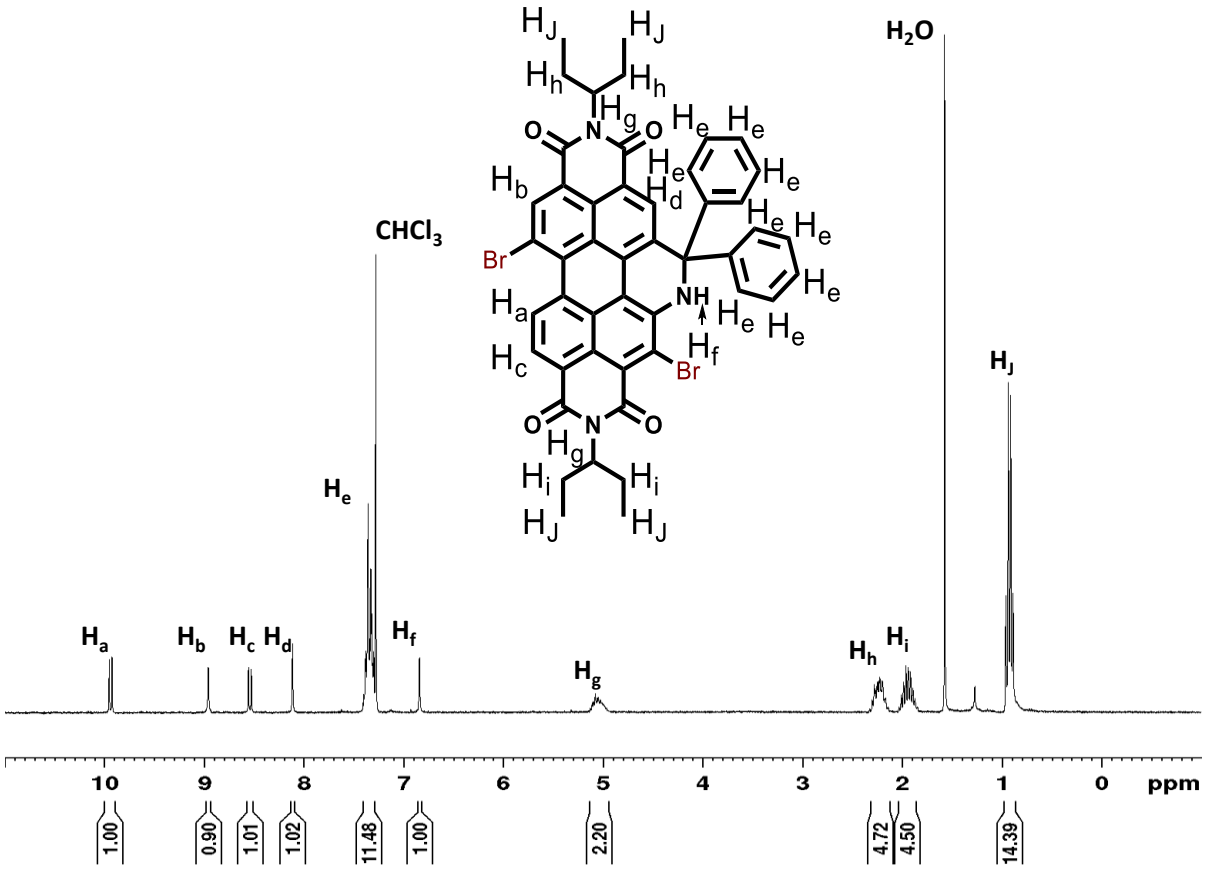

Figure 30: ^{1}H-NMR spectrum of **6** in $CDCl_3$ recorded at 300 MHz.

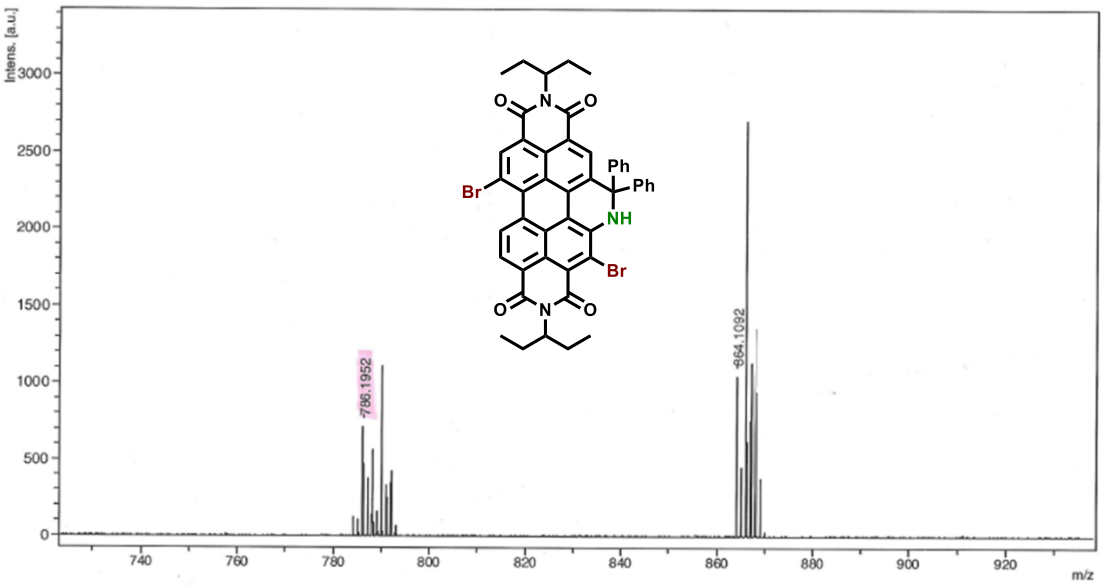

Figure 31: MALDI-TOF Mass spectrum of **6**

5. Conclusion

We report the synthesis of an alcohol/amine solvent soluble n-type PDI semiconductor (**X1**) exhibiting electron mobilities of 10^{-5} cm^2 V^{-1} s^{-1}. **X1** was characterized by: optical absorption spectroscopy, CV, single crystal XRD, ^{1}H-NMR, ^{13}C-NMR, MALDI-TOF mass spectrometry, CHN elemental analysis, TGA and DSC. The new PDI incorporates a cyclic secondary amine at the bay position. The added NH functional group destabilizes the frontier molecular orbitals energy levels and leads to significant red shifting of the optical absorption, compared to the parent PDI chromophore owing to electron donation from the secondary amine. The NH group also enables green solvent processing (via alcohol/amine mixtures) to produce spin-cast thin-films capable of electron transport. Higher electron mobility and air stable OFET operation are required for practical use.

Next generation molecules have been defined (**X2-X6**) and will target installation of electron withdrawing groups on the opposite bay position(s) and on the ketone precursor to increase electron affinity (and lower the pK_a of the NH for more facile deprotonation). DFT analysis of possible structures has provided information on LUMO and HOMO energy levels of the targets. Targets **X2**(72%) and **X4**(24%) were synthesized successfully and characterized by ^{1}H-NMR spectroscopy and MALDI-TOF HRMS. An unexpected discovery was made in the synthesis of **6**. Instead of accessing a mono-brominated product we have succeeded in synthesizing a dibrominated **X1** derivative with bromo substituents at the opposite bay position and headland position adjacent to the N-H moiety. This is exciting as it can provide a quick synthetic route to headland substituted PDI derivatives. The substitution of the headland position of PDI with an aryl bromide allows for the conversion to cyano substituted PDI **X6**, and additionally it provides an

opportunity to perform metal-catalyzed cross coupling reactions at the headland position to synthesize unique PDI analogues.

There are several considerations that the synthesis of **X1** raises with respect to optimization. Upon inspection of the optimization data it appears that the equivalents of TfOH may not have been fully optimized. Despite obtaining a good yield (84%) various equivalents of TfOH were not tried. Most notably it would be interesting to see how the reaction would proceed with a stoichiometric amount of TfOH. Another point to contend with the optimization is the selection of solvent. There was only one solvent tried (*o*-xylene) due to its desirable high boiling point, however it may be advantageous to further optimize the solvent choice to improve the solubility of future substrates. While *o*-xylene provided sufficient solubility character for the reagents in these reactions, it was observed that the solubility was poor before heating was commenced. This may present a problem with reaction mixtures containing more polar substituents.

The synthetic method was unsuccessful with alkyl and haloalkyl ketone precursors, products **2** and **3** respectively. This presents a synthetic challenge to explore the reaction conditions needed to expand the scope of the reaction. It is postulated within that the initial formation of an oxocarbenium intermediate may be a pivotal step in the reaction. Experiments to find new conditions which stabilize this intermediate will likely be successful in determining possible ways to expand the substrate scope. An early speculation is that the addition of more equivalents of acid catalyst may promote the formation of the necessary oxocarbenium ion.

Future work will focus on completing the synthesis and advanced optoelectronic characterization of **X3, X5,** and **X6**. It is shown that the synthetic method can be applied to substituted aryl ketones which leads to the possibility of various targets with differing aryl substituents to those shown previously. For instance, nitro substituted ketones could be an

attractive addition to the target list since they affect strong electron withdrawing character. There are various other examples of aryl substituted ketones which could also be explored. Bis-ketones are another class of molecules that would be interesting to explore in this reaction. The ability to synthesize asymmetric products would be possible by using bis-ketones. This thesis has provided a foundation for an extraordinary emergence of new synthetic chemistry from the Welch laboratory.

Appendix 1: Synthesis and Characterization

a) Materials and Methods

Materials: All reagents and solvents were purchased from Millipore-Sigma and used without further purification.

Nuclear Magnetic Resonance (NMR): ^{1}H and ^{13}C NMR spectroscopy experiments were recorded using a Bruker Avance III 500 MHz spectrometer. All experiments were performed in chloroform-d ($CDCl_3$). Chemical shifts (referenced to residual solvent) were reported in parts per million (ppm). Multiplicities were reported as follows: singlet (s), doublet of doublets (dd), and multiplets (m).

High-resolution Mass Spectrometry (HRMS): High-resolution MALDI mass spectrometry measurements were performed courtesy of Johnson Li in the Chemical Instrumentation Facility at the University of Calgary. A Bruker Autoflex III Smartbeam MALDI-TOF (Na:YAG laser, 355 nm), setting in positive reflective mode, was used to acquire spectra.

CHN Elemental Analysis: Elemental analyses were performed by Johnson Li in the Chemical Instrumentation Facility at the University of Calgary (UofC). A Perkin Elmer 2400 Series II CHN Elemental Analyzer was used to obtain CHN data, using ~1.5 mg of sample (with particle sizes ranging between 0.2 and 0.5 mm in diameter).

UV-Visible Spectroscopy (UV-Vis): All optical absorption measurements were recorded using Agilent Technologies Cary 60 UV-Vis spectrometer at room temperature. All solution UV-Vis experiments were run using 2 mm quartz cuvettes. Stock solutions (1.0 mg/mL) of each compound were prepared in $CHCl_3$, serially diluted to concentrations between 10^{-5} - 10^{-6} M, and then used to construct calibration curves for determining molar absorptivity. Neat films were prepared from $CHCl_3$ solutions by spin-coating from a 1 % wt/v solution onto clean Corning glass micro slides.

Alcohol processed thin films were cast from 40 μL of a 5 mg/mL solution of **X1** in 1:1 *n*-propanol:*n*-butylamine. Alcohol processed solution optical absorbance measurements were recorded for 10^{-5} M solutions of **X1** in 1:1 *n*-propanol:*n*-butylamine. Prior to use, glass slides were cleaned with acetone and isopropanol, followed by UV/ozone treatment using a Novascan UV/ozone cleaning system.

Cyclic Voltammetry (CV): Electrochemical measurements were performed using a CH Instruments Inc. Model 1200B Series Handheld Potentiostat. A standard 3-electrode setup was utilized, consisting of a freshly polished glassy carbon disk working electrode (WE), Pt-wire counter electrode (CE), and Ag-wire pseudo-reference electrode (RE). All measurements were referenced to ferrocene (Fc+/0) as internal standard. All cyclic voltammetry experiments were performed at a scan rate of 100 mV/s. Sample solutions, with 1 mM compound and 0.1 M tetrabutylammonium hexafluorophosphate ($TBAPF_6$) supporting electrolyte, were prepared in anhydrous dichloromethane. All electrochemical solutions were sparged with dry gas (either N_2 or argon) for 5 minutes to deoxygenate the system prior to measurements.

Single Crystal XRD: Single crystals of $C_{55}H_{49}N_3O_4$, **X1**, were grown from *o*-xylene (1 mL) and hexanes (1 mL) at 298K. A suitable crystal was selected and mounted on a glass loop using Paratone oil. Diffraction experiments were performed on a Bruker Smart diffractometer equipped with an Incoatec Microfocus (Cu Kα, λ = 1.54178 Å) and an APEX II CCD detector. The crystal was kept at 173 K during data collection. Diffractions spots were integrated and scaled with SAINT[65] and the space group was determined with XPREP[66]. Using Olex2[67], the structure was solved with the ShelXT[68] structure solution program using Intrinsic Phasing and refined with the ShelXL[69] refinement package using Least Squares minimization.

Organic Field Effect Transistors: Fabrication: Si/SiO_2 substrates with patterned Au contacts (bottom-gate bottom-contact) were purchased from Fraunhofer IPMS, having channel lengths from 2.5 to 20 µm, channel width of 2000 µm and dielectric thickness of 230 nm. The substrates were plasma treated for 10 minutes, then surface-functionalized with octyltrichlorosilane (1% v/v in toluene) for one hour. X1 was dissolved in 1:1 isopropanol/n-butylamine or n-propanol/n-butylamine solutions at 5 mg/mL. These solutions were then spin-coated at 1000 rpm for 60 seconds onto the treated substrates in an inert atmosphere.

Characterization: Devices were characterized under vacuum (< 0.1 Pa) in a custom oesProbe A10000-P290 system (Element Instrumentation Inc. & Kreus Design Inc.). A Keithley 2614B was used to modulate the gate-source voltage (V_{GS}) and source-drain voltage (V_{DS}) and measure the source-drain current (I_{DS}). A constant V_{DS} of 70 V was used to obtain the saturation field-effect electron mobility and threshold voltage over a V_{GS} range of 0 to 100 V.

Calculation of Electron Mobility:

The relationship between I_{DS} and V_{GS} in the saturation region are given in **Equation 1**:

$$(1)\ I_{DS} = \frac{\mu C_i W}{2L}(V_{GS} - V_T)^2$$

Where C_i is the capacitance of the gate dielectric (1.5×10^{-4} F m^{-2}), µ is the field-effect electron mobility of the material, V_T is the threshold voltage, W is the width of the channel, and L is the length of the channel.

To find the mobility, the equation can be rearranged by taking the square root, giving **Equation 2**:

$$(2)\ \sqrt{I_{DS}} = \sqrt{\frac{\mu C_i W}{2L}}(V_{GS} - V_T)$$

This gives a linear relationship between $\sqrt{I_{DS}}$ and V_{GS}. The slope of linear region of the $\sqrt{I_{DS}}$ vs V_{GS} curve gives $\sqrt{\frac{\mu C_i W}{2L}}$, which all constants are known except μ, for which we can solve. V_T is simply the x-intercept of this line.

b) X1 Synthesis: Experimental Procedure

Benzophenone (29 mg, 0.16 mmol, 1.6 eq.) was added to a 10 mL pressure tube equipped with a stir bar. *o*-Xylene (2 mL) was added, followed by trifluoromethanesulfonic acid (7.8 μL, 0.09 mmol, 0.9 eq.), and the mixture was stirred for 5 minutes. Compound **1** (54 mg, 0.10 mmol, 1.0 eq.) was added, the vial was sealed, and the reaction was heated at 165 ºC for 24 hrs. During the reaction the solution changed from a dark red colour to dark green. The reaction mixture was poured into a 250 mL separatory funnel and diluted with 35 mL of Ethyl Acetate. The organic layer was washed twice with saturated $NaHCO_3$(aq) to neutralize residual acid and once with brine. The organic layer was collected, dried with anhydrous $MgSO_4$, and gravity filtered into a 250 mL round bottom flask. The solvent was removed *in vacuo* and the resulting crude solid was dissolved in 30 mL of dichloromethane and passed through a Silica plug eluting with dichloromethane to separate the product from excess benzophenone. The green band was collected, and the solvent was removed *in vacuo*. The resulting dark green solid was precipitated with a 1:3 MeOH:H_2O solution (the product was found to be partially soluble in 100% MeOH) and collected via vacuum filtration. Compound **X1** was obtained in 84% yield (59 mg, 0.084 mmol).

^{1}H NMR (500 MHz, $CDCl_3$, 27 ºC): δ 8.55 (m, 1H, Ha), 8.57 (dd, J = 8.0 Hz, 2H, Hb), 8.41 (m, 1H, Hc), 8.09 (m, J = 8.3 Hz, 1H, Hd), 7.37 (m, J , 8H, He), 7.32 (m, 2H, Hf), 5.69 (s, 1H, Hg), 5.01 (s, 1H, Hh), 2.22 (m, 4H, Hi), 1.90 (m, 4H, Hj), 0.89 (m, 12H, Hk).

^{13}C NMR (151 MHz, $CDCl_3$, 27 ºC): δ 144.8, 140.8, 135.4, 131.6, 130.5, 128.7, 128.3, 127.6, 125.6, 124.6, 123.2, 122.9, 121.3, 112.6, 67.9, 57.1, 57.0, 24.5, 24.4, 10.9, 10.7.

UV-Vis λ (M^{-1} cm^{-1}): 433 nm (18629), 651 nm (28469)

CHN theoretical (%) C: 79.53, H: 5.54, N: 5.92; found (%) C: 78.83; H: 5.75; N: 5.92

c) CHN Elemental Analysis of X1

Figure A1-1 displays the CHN elemental analysis results for **X1**. The largest deviation from the theoretical value is ≈0.7% which leads one to conclude that the sample is reasonably pure.

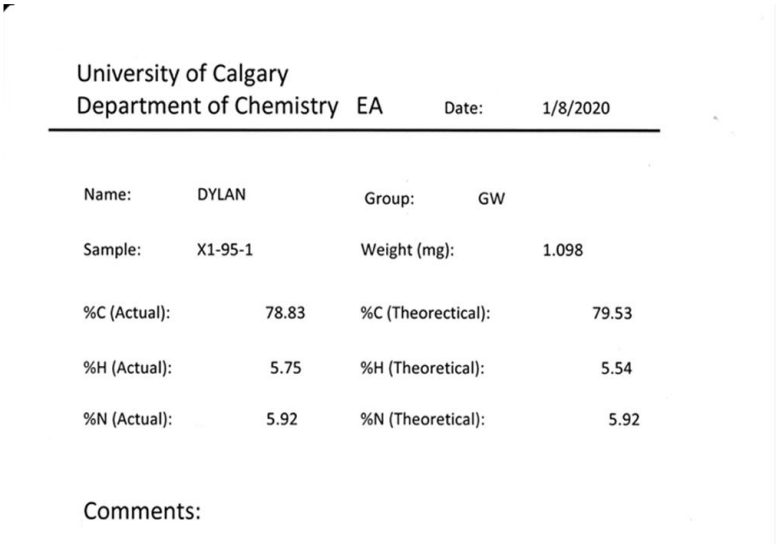

University of Calgary
Department of Chemistry EA Date: 1/8/2020

Name:	DYLAN	Group:	GW
Sample:	X1-95-1	Weight (mg):	1.098
%C (Actual):	78.83	%C (Theorectical):	79.53
%H (Actual):	5.75	%H (Theoretical):	5.54
%N (Actual):	5.92	%N (Theoretical):	5.92

Comments:

Figure A1-1: CHN Elemental Analysis results for **X1**

d) High Resolution Mass Spectrometry of X1

Figure A1-2 shows the MALDI-TOF HRMS of **X1**. The HRMS ([M-2H]+H^+) calculated for $C_{47}H_{38}N_3O_4$: 708.2857; detected [M-2H]+H^+: 708.2861

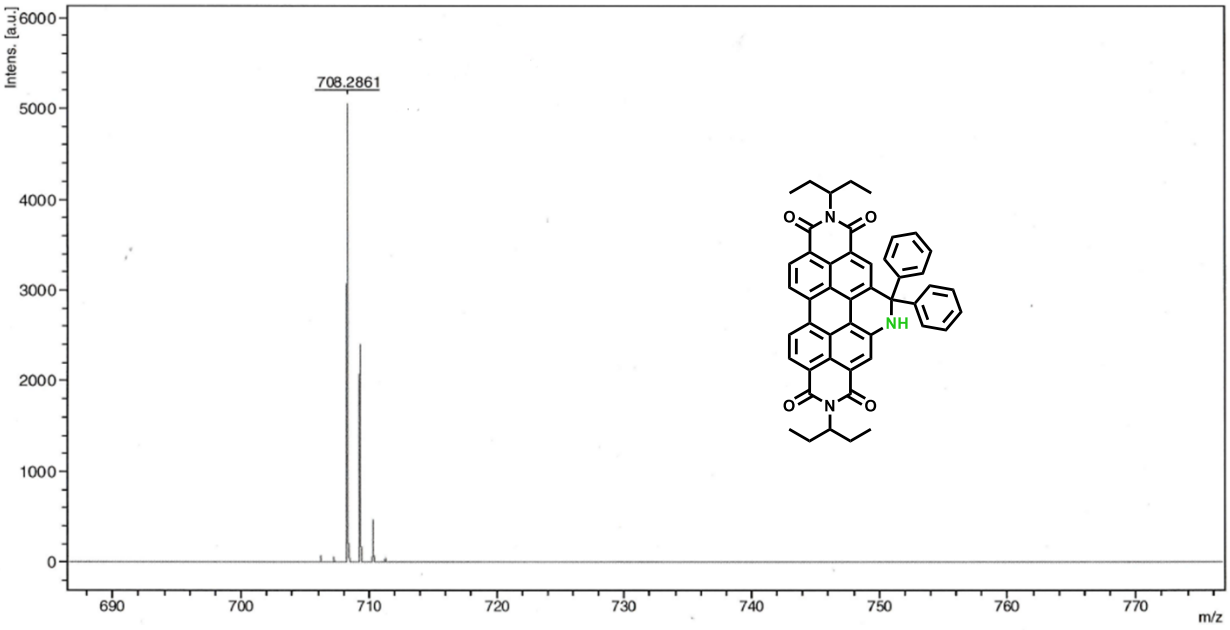

Figure A1-2: MALDI-TOF Mass Spectrum of **X1**

e) High Resolution Mass Spectrometry of X2

Figure A1-3 shows the MALDI-TOF HRMS of **X2**. The HRMS ([M-2H]+H^+) calculated for $C_{47}H_{37}Br_2N_3O_4$: 864.1151; detected [M-2H]+H^+: 864.1024.

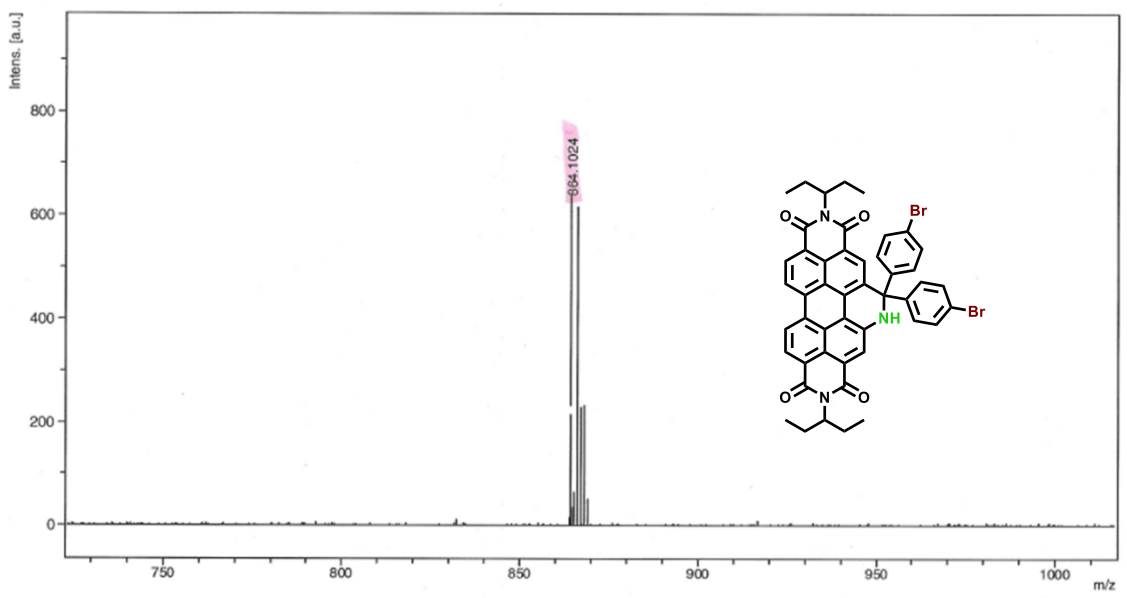

Figure A1-3: MALDI-TOF HRMS of **X2**

Appendix 2: Synthesis of a Ring-Fused PDI Dimer

a) Motivation

The following work was completed at the beginning of my MSc and was concluded approximately 8 months into the program. My first project was focused on developing new π-conjugated molecules using DHA methods. Figure A2-1 displays literature precedent for the synthesis of ring-fused PDI compounds. The Nuckolls laboratory synthesized the product on the left and at the time it was a top performing material for OPV as well as OFETs. This was motivational for us to begin the synthesis of ring-fused PDIs. The introduction of various heteroatoms on the ring-fused core could be used to vary the optoelectronic properties of the final target. The synthesis of the Nuckolls target[70,71] involves Stille coupling, which is a method that we would like to avoid under the umbrella of green chemistry. Stille coupling has been avoided in the synthesis of other similar targets.[72,73] We will attempt to implement DHA reactions[74,75] in order to reduce the environmental impact of the synthesis.

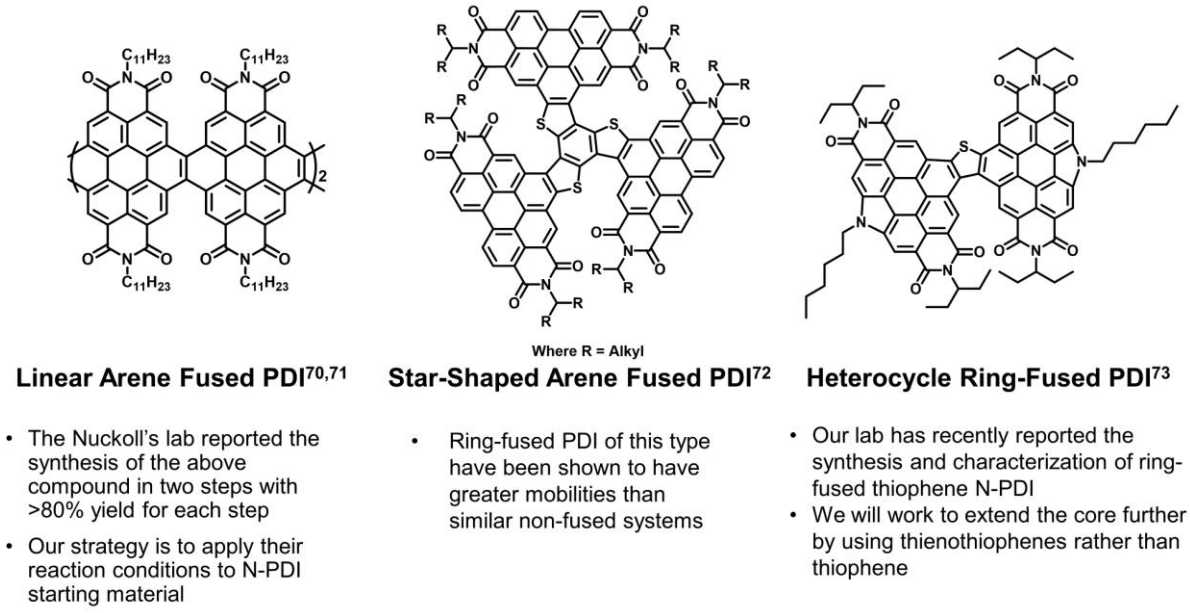

Figure A2-1: Literature Precedent for the Synthesis of Ring-Fused PDIs

b) Design

Figure A2-2 displays the synthetic targets for the ring-fusion synthesis. Targets 1 and 2 are very similar to the literature precedent discussed earlier while Targets 3 and 4 are more ambitious and the plan was to only try to synthesize Targets 3 and 4 if the initial synthesis was successful.

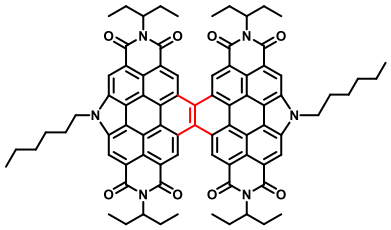

Target 1

- Our initial target is simple and practical in design and synthesis – this structure works!
- Green synthesis, pyrrolic N-sites for extra side chains to enhance printability

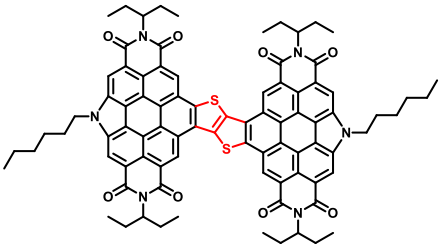

Target 2

- Ring-fused thienothiophene N-annulated PDI has yet to be investigated
- Synthesis involves Direct Heteroarylation (DHA)
- Our hypothesis is that the insertion of thienothiophene (instead of thiophene) will produce a more planar product

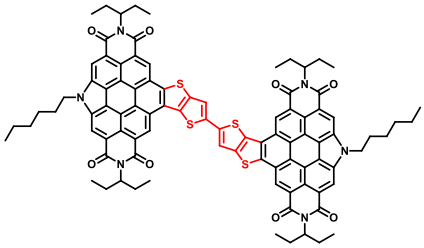

Target 3

- This target is analogous to the last thienothiophene target, except the core of the molecule is further extended

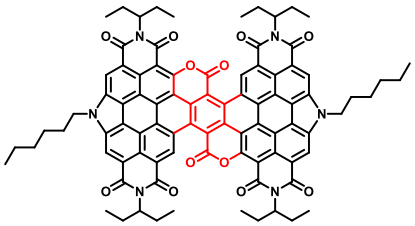

Target 4

- This target incorporates ring fused ester moieties into N-PDI framework and should increase molecular polarity, solubility, and intermolecular interactions → easily made

Figure A2-2: Synthetic targets for ring-fusion synthesis

c) Attempted Synthesis

The DHA was unsuccessful after many tries with various substrates, therefore we resorted to the use of Stille coupling. Though a very robust reaction, Stille coupling is not desirable due to detrimental environmental impact. Figure A2-3 shows the catalytic cycle of the Stille coupling. Two equivalents of $BrSnMe_3$ are produced (one at each transmetallation) which is the reason why the Still coupling is environmentally detrimental. Alkyl tin species are historically known for their

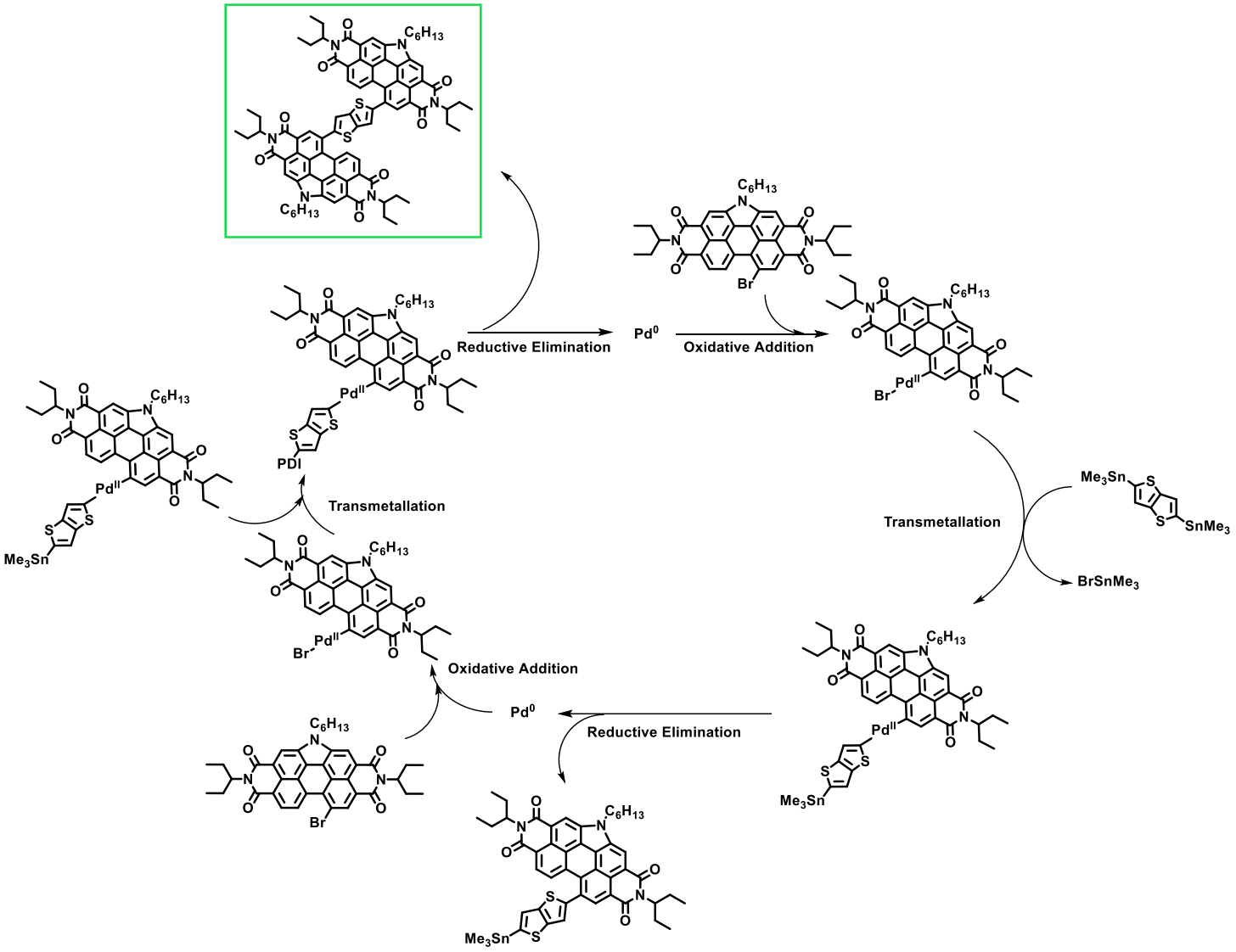

Figure A2-3: Representative Stille coupling catalytic cycle for Target 2

toxicity to all types of life. The catalytic cycle is shown for Target 2 however it is applicable for other targets as well. This method was used to synthesize PDI species acting as precursors to ring fused PDIs.

Figure A2-4 shows the attempted synthesis of Target 1. The Scholl reaction was unsuccessful in fully cyclizing the molecule. Rather a 'half-cyclized' product was formed. Key points from this reaction include:

- The reaction did not form the desired product
- Instead it selectively formed the 'half-cyclized' product
- The work-up ^{1}H-NMR had only baseline impurities
- The reaction could be run again in a higher boiling solvent at a higher temperature in order to form the desired product

Figure A2-5 displays the ^{1}H-NMR spectrum of the 'half-cyclized' product. Integration of 10 for the aromatic region is the most striking identifier that the 'half-cyclized' product was formed.

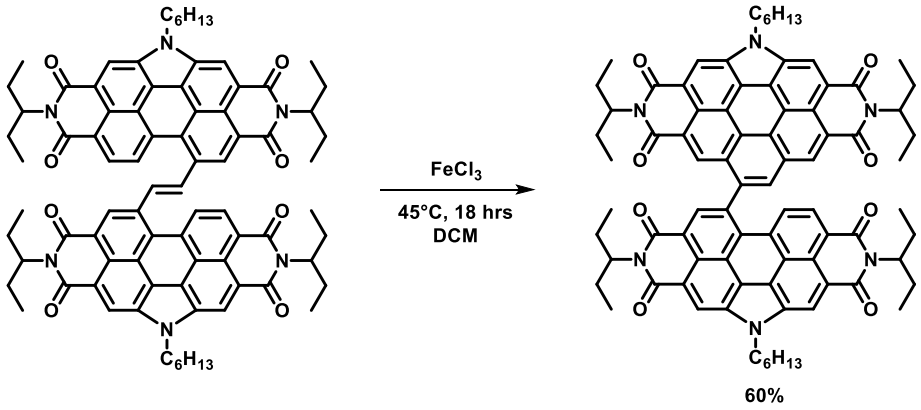

Figure A2-4: Attempted synthesis of Target 1

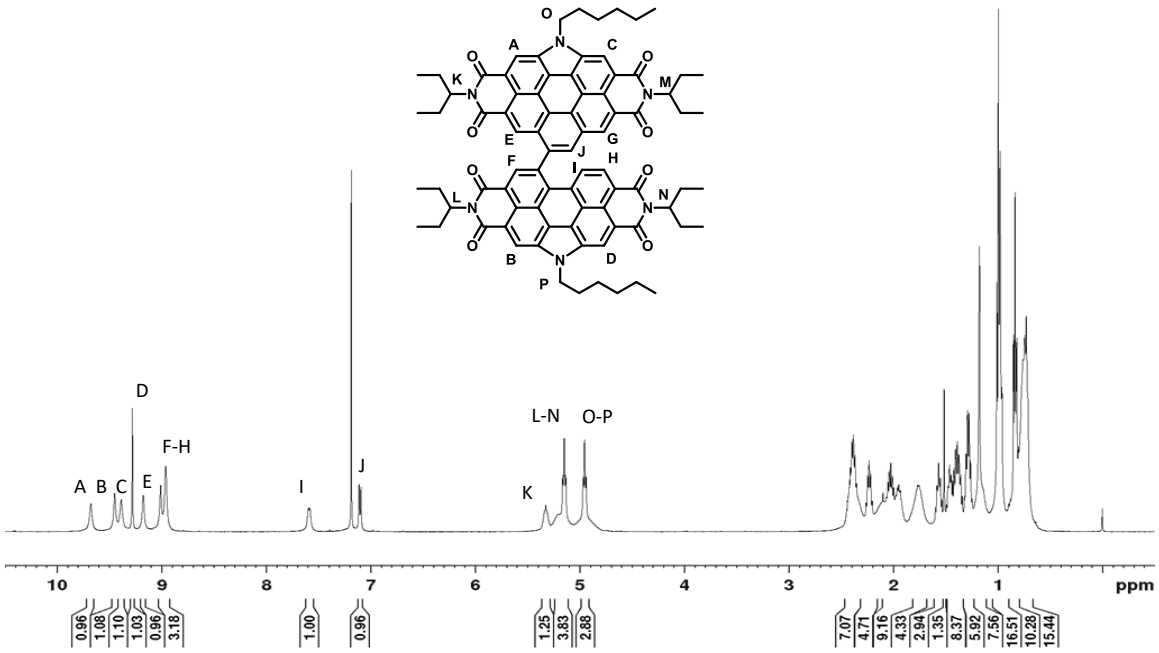

Figure A2-5: ^{1}H-NMR spectrum of the 'half-cyclized' product in $CDCl_3$ recorded at 500 MHz.

Figure A2-6 displays a representative ^{1}H-NMR of the Stille coupling products synthesized in this project. The diagnostic peak in this spectrum can be found at ≈7.8 ppm where a singlet

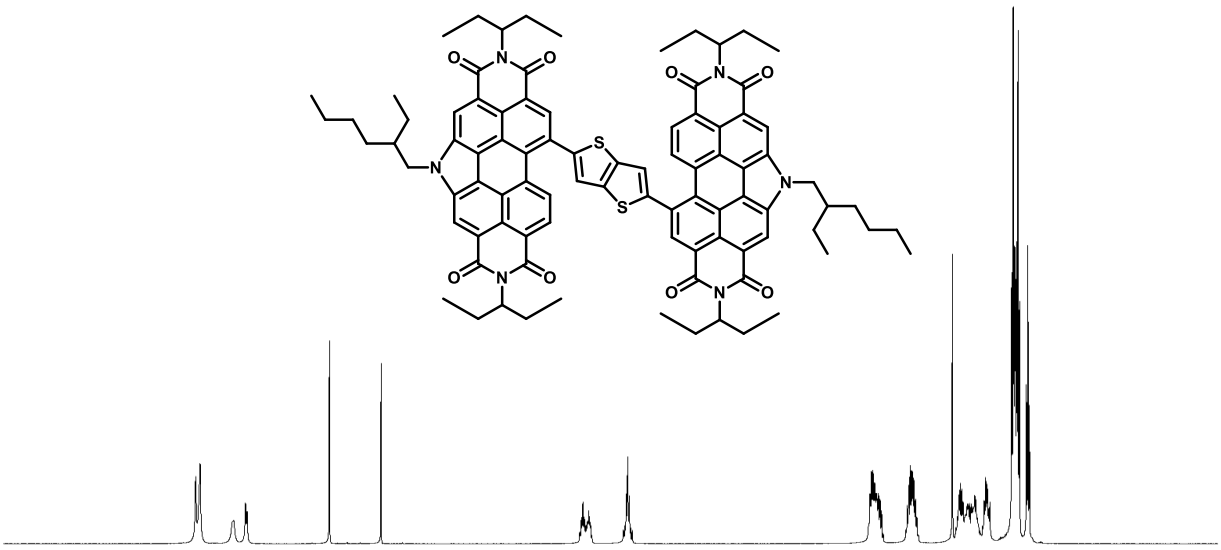

Figure A2-6: ^{1}H-NMR spectrum of a representative Stille coupling product shown in $CDCl_3$ at 500 MHz.

integrating to 2 hydrogens is found. This peak corresponds to the two remaining hydrogens on the thienothiophene precursor. This product was also confirmed by MALDI-TOF HRMS.

Attempted ring-fusion synthesis is shown in Figure A2-7. Important points include:

- The product of this reaction was not soluble in benzene, THF, hexanes, acetone, *o*-dichlorobenzene, DCM, or chloroform
- A NMR spectrum was not able to be obtained. MALDI-TOF Mass Spectrometry confirmed the formation of the product, and the depletion of the PDI-Thienothiophene-PDI starting material

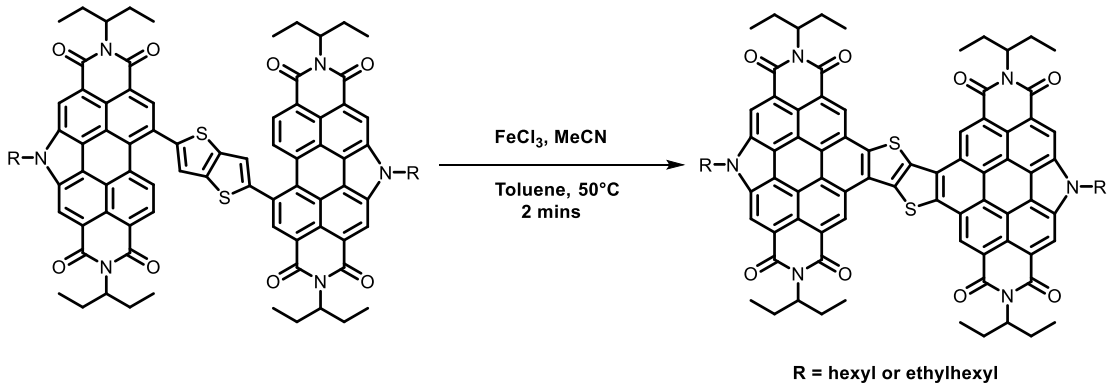

Figure A2-7: Attempted ring-fusion synthesis using previously established reaction conditions.[68]

d) Conclusion

- Our original hypothesis that Target 2 would be soluble enough for processing into thin films was proven to be false
- Moving forward ring-fused compounds will need to be synthesized with much larger imide chains in order to enhance the solubility (As seen in the Nuckolls example)
- Product **2** was synthesized in decent yield and it is possible that it could be a viable charge-transport material even without ring fusion
- Project was halted due to concerns that final products will not have desirable solubility characteristics (Target 3 and 4 synthesis not attempted)

References

1 - Y. Zhong, B. Kumar, S. Oh, M. T. Trinh, Y. Wu, K. Elbert, P. Li, X. Zhu, S. Xiao, F. Ng, M. L. Steigerwald and C. Nuckolls. *J. Am. Chem. Soc.*, 2014, **136** (22), 8122-8130.

2 - Y. Zhong, M. T. Trinh, R. Chen, G. E. Purdum, P. P. Khlyabich, M. Sezen, S. Oh, H. Zhu, B. Fowler, B. Zhang, W. Wang, C. Y. Nam, M. Y. Sfeir, C. T. Black, M. L. Steigerwald, Y. L. Loo, F. Ng, X. Y. Zhu and C. Nuckolls. *Nat. Commun.*, 2015, **6** (1), 1-8.

3 - J.D. Oh, E.S. Shin, D. K. Kim and J. H. Choi. *Synth. Met.*, 2016, **220**, 421-427.

4 - F. Chianese, A. Candini, M. Affronte, N. Mishra, C. Coletti and A. Cassinese. *Appl. Phys. Lett.*, 2018, **112** (21), 213301.

5 - A. Nowak-Król and F. Würthner. *Org. Chem. Front.*, 2019, **6** (8), 1272-1318.

6 - C. Huang, S. Barlow and S. R. Marder. *J. Org. Chem.*, 2011, **76**, 2386-2407.

7 - A. Nowak-Król, K. Shoyama, M. Stolte and F. Würthner. *Chem. Commun.*, 2018, **54** (98), 13763-13772.

8 – P. Rajasingh, R. Cohen, E. Shirman, L. J. W. Shimon and B. Rybtchinski. *J. Org. Chem.*, 2007, **72** (16), 5973–5979.

9 – F. Würthner, V. Stepanenko, Z. Chen, C. R. Saha-Möller, N. Kocher and D. Stalke. *J. Org. Chem.*, 2004, **69** (23), 7933–7939.

10 - B.A. Jones, A. Facchetti, M. R. Wasielewski and T.J. Marks. *J. Am. Chem. Soc.*, 2007, **129** (49), 15259-15278.

11 - R. T. Weitz, K. Amsharov, U. Zschieschang, E.B. Villas, D. K. Goswami, M. Burghard, H. Dosch, M. Jansen, K. Kern and H. Klauk. *J. Am. Chem. Soc.*, 2008, **130**, 4637-4645.

12 - J.H. Oh, Y.S. Sun, R. Schmidt, M. F. Toney, D. Nordlund, M. Konemann, F. Würthner and Z. Bao. *Chem. Mater.*, 2009, **21**, 5508-5518.

13 - J. Zhang, J. Jin, H. Xu, Q. Zhang and W. Huang. *J. Mater. Chem. C.*, 2018, **6** (14), 3485-3498.

14 - W. Tang, Y. Huang, Lei Han, R. Liu, Y. Su, X. Guo and F. Yan. *J. Mater. Chem. C.*, 2019, **7**, 790-808.

15 - G. Schweicher, G. Garbay, R. Jouclas, F. Vibert, F. Devaux and Y. H. Geerts. *Adv. Mater.*, 2020, **32** (10), 1905909.

16 - Z. B. Henson, P. Zalar, X. Chen, G. C. Welch, T. Q. Nguyen and G. C. Bazan. *J. Mater. Chem. A.*, 2013, **1** (37), 11117-11120.

17 - H. Usta, A. Facchetti and T. J. Marks. *Acc. Chem. Res.*, 2011, **44** (7), 501-510.

18 - C. Piliego, D. Jarzab, G. Gigli, Z. Chen, A. Facchetti and M. A. Loi. *Adv. Mater.*, 2009, **21** (16), 1573-1576.

19 - Z. He, S. Shaik, S. Bi, J. Chen and D. Li. *Appl. Phys. Lett.*, 2015, **106** (18), 183301.

20 – L. Hao, W. Jiang and Z. Wang. *Tetrahedron*, **68** (2012) 9234-9239.

21 – M. Schulze, A. Steffen and F. Würthner. *Angew. Chem. Int. Ed.*, 2015, **54** (5), 1570–1573.

22 – M. Schulze, M. Philipp, W. Waigel, D. Schmidt and F. Würthner. *J. Org. Chem.*, 2016, **81** (18), 8394–8405.

23 – A. Goujon, L. Rocard, T. Cauchy and P. Hudhomme. *J. Org. Chem.*, 2020, **85** (11), 7218–7224.

24 - 32 - G. Li, Y. Zhao, J. Li, J. Cao, J. Zhu, X. W. Sun and Q. Zhang. *J. Org. Chem.*, 2015, **80**, 196-203.

25 - M. Adachi and Y. Nagao. *Chem. Mater.*, 2001, **13**, 662−669.

26 – N. Nijegorodov, R. Mabbs, and W. S. Downey. *Spectrochim. Acta, Part A*, 2001, **57**, 2673−2685.

27 – Y. Avlasevich, C. Li and K. Mullen. *J. Mater. Chem.*, 2010, **20**, 3814−3826

28 - H. Langhals and S. Kirner. *Eur. J. Org. Chem*., 2000, **2000**, 365-380.

29 - A. D. Hendsbee, J.P. Sun, W.K. Law, H. Yan, I. G. Hill, D. M. Spasyuk and G. C. Welch. *Chem. Mater*., 2016, **28**, 19, 7098-7109.

30 - S. M. McAfee, S. V. Dayneko, P. Josse, P. Blanchard, C. Cabanetos and G. C. Welch. *Chem. Mater.*, 2017, **29** (3), 1309-1314.

31 - M. Nazari, M. A. Martell, T. A. Welsh, O. Melville, Z. Li, J. R. Cann, E. Cieplechowicz, Y. Zou, B. H. Lessard and G. C. Welch. *Mater. Chem. Front.*, 2018, **2** (12), 2272-2276.

32 - M. Nazari, E. Cieplechowicz, T. A. Welsh and G. C. Welch. *New J. Chem.*, 2019, **43** (13), 5187-5195.

33 - A.D. Hendsbee, S.V. Dayneko, J.A. Pells, J.R. Cann and G. C. Welch. *Sustain. Energy Fuels*, 2017, **1** (5), 1137-1147.

34- M. Vespa, J. R. Cann, S. V. Dayneko, O. A. Melville, A. D. Hendsbee, Y. Zou, B. H. Lessard and G. C. Welch. *Eur. J. Org. Chem.*, 2018, **2018** (33), 4592-4599.

35 – S. V. Dayneko, A. D. Hendsbee and G. C. Welch. *Small Methods*, 2018, **2** (6), 1800081.

36 - K. H. Cheon, H. Ahn, J. Cho, H. J. Yun, B. T. Lim, D. J. Yun, H. K. Lee, S. K. Kwon, Y. H. Kim and D. S. Chung. *Adv. Funct. Mater.*, 2015, **25** (30), 4844-4850.

37 - B. Schmatz, Z. Yuan, A. W. Lang, J. L. Hernandez, E. Reichmanis and J. R. Reynolds. *ACS Cent. Sci*., 2017, **3** (9), 961-967.

38 - D. Ho, J. Lee, S. Park, Y. Park, K. Cho, F. Campana, D. Lanari, A. Facchetti, S. Seo, C. Kim, A. Marrocchi, and L. Vaccaro. *J. Mater. Chem. C.*, 2020, **8** (17), 5786-5794.

39 - C.J. Clarke, W.C. Tu, O. Levers, A. Bröhl and J.P. Hallett. *Chem. Rev.*, 2018, **118** (2), 747-800.

40 - A. Marrocchi, A. Facchetti, D. Lanari, C. Petrucci and L. Vaccaro. *Energy Environ. Sci.*, 2016, **9** (3), 763-786.

41 - B. V. Khau, L. R. Savagian, M. De Keersmaecker, M. A. Gonzalez and E. Reichmanis. *ACS Materials Lett.*, 2019, **1** (6), 599-605.

42 - B. Kang, Z. Wu, M.J. Kim, H.Y. Woo and J.H. Cho. *Chem. Mater.*, 2020, **32** (3), 1111-1119.

43 – F. May, V. Marcon, M. R. Hansen, F. Grozema and D. Andrienko. *J. Mater. Chem.*, 2011, **21** (26), 9538.

44 – C. Song, X. Liu, X. Li, Y.-C. Wang, L. Wan, X. Sun, W. Zhang and J. Fang. *ACS Appl. Mater. Interfaces*, 2018, **10** (17), 14986–14992.

45 - C. R. Harding, J. Cann, A. Laventure, M. Sadeghianlemraski, M. Abd-Ellah, K. R. Rao, B. S. Gelfand, H. Aziz, L. Kaake, C. Risko and G. C. Welch. *Mater. Horiz.*, 2020, **7** (11), 2959–2969.

46 - B. V. Khau, L. R. Savagian, M. De Keersmaecker, M. A. Gonzalez and E. Reichmanis. *ACS Materials Lett.*, 2019, **1** (6), 599-605.

47 - T. H. Reilly, A. W. Hains, H.Y. Chen and B. A. Gregg. *Adv. Energy Mater.*, 2012, **2** (4), 455-460.

48 - B. Russ, M. J. Robb, F. G. Brunetti, P. L. Miller, E. E. Perry, S. N. Patel, V. Ho, W. B. Chang, J. J. Urban, M. L. Chabinyc, C. J. Hawker and R. A. Segalman. *Adv. Mater.*, 2014, **26** (21), 3473-3477.

49 – Z. B. Henson, P. Zalar, X. Chen, G. C. Welch, T. -Q. Nguyen and G. C. Bazan. *J. Mater. Chem. A*, 2013, **1** (37), 11117.

50 – J. Yang, A. Garcia and T.-Q. Nguyen, T. -Q. *Appl. Phys. Lett.*, 2007, **90** (10), 103514.

51 – F. Huang, Y. Zhang, M. S. Liu, and A. K.-Y. Jen. *Adv. Funct. Mater.*, 2009, **19** (15), 2457–2466.

52 – K. Lu, Y. Guo, Y. Liu, C. Di, T. Li, Z. Wei, G. Yu, C. Du, and S. Ye. *Macromolecules*, 2009, **42** (9), 3222–3226.

53 - H.Y. Tsai and K.Y. Chen. *Dyes Pigm.*, 2013, **96** (2), 319-327.

54 - C. Domínguez, M.J. Baena, S. Coco and P. Espinet. *Dyes Pigm.*, 2017, **140**, 375-383.

55 - D. H. Harris, S. Brixi, B. S. Gelfand, B. H. Lessard and G. C. Welch. *J. Mater. Chem. C*, 2020, **8** (29), 9811–9815.

56 - B. Grimm, C. Risko, J. D. Azoulay, J.L Bredas and G.C. Bazan. *Chem. Sci.*, 2013, **4**, 1807.

57 - S. Nakamura, M. Tanaka, T. Taniguchi, M. Uchiyama and T. Ohwada. *Org. Lett.*, 2003, **5** (12), 2087.2090.

58 - M. J. Ahrens, M. J. Tauber and M. R. Wasielewski. *J. Org. Chem.*, 2006, **71** (5), 2107.2114.

59 - O. A. Melville, T. M. Grant, K. Lochhead, B. King, R. Ambrose, N. A. Rice, N. T. Boileau, A. Peltekoff, M. N. Tousignant, I. G. Hill and B. H. Lessard. *ACS Appl. Electron. Mater.*, 2020. **2**, (5), 1313-1322.

60 – *CRC Handbook of Chemistry and Physics*. CRC Press: Cleveland, Ohio 1977.

61 – I. P. Beletskaya and A. V. Cheprakov. *Chem. Rev.*, 2000, **100** (8), 3009–3066.

62 – C. Cordovilla, C. Bartolomé, J. M. Martínez-Ilarduya and P. Espinet, P. *ACS Catal.*, 2015, **5** (5), 3040–3053.

63 – A. Suzuki. *Angew. Chem. Int. Ed.*, 2011, **50** (30), 6722–6737.

64 - Y. Kumar, S. Kumar, D. Bansal and P. Mukhopadhyay. *Org. Lett*,. 2019, **21** (7), 2185–2188.

65 - Bruker-AXS. SAINT; Madison, Wisconsin, USA, 2017.

66 - Bruker-AXS. XPREP; Madison, Wisconsin, USA, 2017.

67 – O. V. Dolomanov, L. J. Bourhis, R. J. Gildea, J.A.K. Howard and H. Puschmann. *J. Appl. Cryst.*, 2009. **42**, 339-341.

68 – G. M. Sheldrick. *Acta. Cryst.,* 2015, **A71**, 3-8.

69 – G. M. Sheldrick. *Acta. Cryst.,* 2015, **C71**, 3-8.

70 – Y. Zhong, M. T. Trinh, R. Chen, G. E. Purdum, P. P. Khlyabich, M. Sezen, S. Oh, H. Zhu, B. Fowler, B. Zhang, W. Wang, C.-Y. Nam, M. Y. Sfeir, C. T. Black, M. L. Steigerwald, Y.-L. Loo, F. Ng, X.-Y. Zhu and C. Nuckolls. *Nat. Comm.*, 2015, **6** (1), 8242.

71 – Y. Zhong, B. Kumar, S. Oh, M. T. Trinh, Y. Wu, K. Elbert, P. Li, X. Zhu, S. Xiao, F. Ng, M. L. Steigerwald and C. Nuckolls. *J. Am. Chem. Soc.,* 2014, **136** (22), 8122–8130.

72 – K. Lin, S. Wang, Z, Wang, Q. Yin, X. Liu, J. Jia, X. Jia, P. Luo, X. Jiang, C. Duan, F. Huang and Y. Cao. *Front. Chem.,* 2018, **6**: 328.

73 – A. Laventure, S. Stanzel, A.-J. Payne, B. H. Lessard and G. C. Welch. *Synthetic Metals,* 2019, **250**, 55–62.

74 – D. J. Schipper and K. Fagnou. *Chem. Mater.,* 2011, **23** (6), 1594–1600.

75 – R. Rossi, F. Bellina, M. Lessi and C. Manzini. *Adv. Synth. Catal.*, 2014, **356** (1), 17–117.